

Chemical changes during endoskarn and porphyry-style alteration and Cu–Fe exoskarn mineralization in the Tonglushan system, eastern China

Fei Zhang^{1,2}  | Ben J. Williamson¹  | Clemens V. Ullmann¹ | Hannah S. R. Hughes¹

¹Camborne School of Mines, University of Exeter, Cornwall, UK

²Zhengzhou Institute of Multipurpose Utilization of Mineral Resources, Zhengzhou, China

Correspondence

Fei Zhang, Camborne School of Mines, University of Exeter, Penryn, Cornwall TR10 9FE, UK.

Email: fzhang_geo@126.com

Funding information

China Scholarship Council, Grant/Award Number: 201706410106

Abstract

Element mobility and chemical mass transfer are evaluated in the formation of Cu–Fe exoskarn deposits and endoskarn and minor porphyry-style alteration in the Tonglushan quartz monzodiorite (QMD) system, eastern China. Endoskarn formation involved the migration of Ca into the QMD from the exoskarnification of carbonates (now marble) xenoliths and wall rocks, addition of Fe and Mn by magmatic-hydrothermal fluids emanating from the interior of the QMD, and removal of alkali elements due to the replacement of feldspars and mica by prograde skarn minerals. Zirconium, Hf, U, and rare earth elements (REE) were added by hydrothermal fluids which were able to carry these often poorly mobile high field strength elements (HFSE) due to elevated F activity. Additions of Al were likely from Na-rich fluids that also caused sodic alteration. Several factors favored mineralization within the exoskarns rather than endoskarns and QMD. The endoskarns were relatively oxidizing, as evidenced by a significant addition of Fe³⁺, which caused Cu to remain in magmatic-hydrothermal fluids until they entered and precipitated sulphides in the more reducing environment of the exoskarns. Fluid migration from the QMD through the endoskarns and into the exoskarns was favored due to decarbonation of wall rock carbonates and related upwards migration of CO₂ to produce a self-sustaining chimney effect, which drew further fluids towards the carbonates to form, alter and mineralize the exoskarns. The higher porosity and permeability of the endoskarns compared with the QMD further promoted the lateral flow of Cu-bearing fluids towards the exoskarns and limited porphyry-style alteration and mineralization within the QMD. This proposed mechanism is only likely to be relevant for porphyry-type systems developed predominantly within carbonate host rocks. Its significance for exploration models is that relatively poorly mineralized porphyry stocks in this setting may be associated with more substantive exoskarn deposits on their margins.

This is an open access article under the terms of the [Creative Commons Attribution-NonCommercial-NoDerivs](https://creativecommons.org/licenses/by-nc-nd/4.0/) License, which permits use and distribution in any medium, provided the original work is properly cited, the use is non-commercial and no modifications or adaptations are made.

© 2023 The Authors. *Resource Geology* published by John Wiley & Sons Australia, Ltd on behalf of Society of Resource Geology.

KEYWORDS

endoskarn, exoskarn, porphyry-style mineralization, element mobility, chemical changes, Tonglushan

1 | INTRODUCTION

Hydrothermal alteration is caused by fluid–rock interactions which accompany the flow of hot aqueous fluids along fractures and grain boundaries under various physicochemical conditions (e.g., Meyer & Hemley, 1967). Geochemical changes caused by hydrothermal alteration can be used to quantify mass transfer during alteration and mineralization, and to determine the behavior and possible sources of the fluids involved (Grant, 1986, 2005).

Isoco analysis, developed by Grant (1986), provides a simple and effective means of quantitatively evaluating chemical gains and losses resulting from mass transfer between precursor rocks and metasomatites (Mathieu, 2018). It has been widely used to study hydrothermal changes associated with mineralization in VMS (e.g., Pilote et al., 2020), SEDEX (e.g., Wilkinson et al., 2011), porphyry (e.g., Tomlinson et al., 2021), IOCG (e.g., Montreuil et al., 2016) and various gold deposit types (e.g., Cail & Cline, 2001), but less commonly in skarns (Dana et al., 2022; Lentz, 2005; Williams-Jones et al., 2010), particularly porphyry-related endoskarns and exoskarns (Karimzadeh Somarin, 2004; Mrozek et al., 2020; Zhao et al., 2022).

Porphyry magmatic systems developed in carbonates are often associated with endoskarns within and exoskarns outside the porphyry intrusion(s) (Einaudi, 1982). Porphyry-style alteration and mineralization is usually considered to be caused by magmatic-hydrothermal fluids derived from the underlying magma chamber (Sillitoe, 2010), whereas endoskarn formation involves extensive chemical exchanges between the porphyry pluton(s) and carbonate wall rocks (Meinert et al., 2005). In general, where endoskarns are widespread, porphyry-type mineralization is poorly developed (Einaudi & Burt, 1982); the reasons for this are not fully understood.

The objective of the current contribution is to address this knowledge gap through the examination of mass changes during the development of endoskarn, exoskarn and porphyry alteration and mineralization in the Tonglushan quartz monzodiorite (QMD) porphyry–skarn system in the Middle-Lower Yangtze River metallogenic belt (MLYRB), eastern China. This system was considered ideal for the study as it hosts ore-barren endoskarns, extensive Cu–Fe exoskarns and only minor porphyry-style alteration and mineralization. The equations of Grant (1986) have been used to evaluate mass changes based on

elements that were immobile during alteration, specifically to quantify addition or depletion of elements during the formation of endoskarn, exoskarn and porphyry-style alteration and mineralization. The overarching aim is to better understand endoskarn formation to aid in the future development of exploration tools to distinguish systems hosting porphyry-type deposits (\pm exoskarns) from those with associated endoskarns and mineralized exoskarns.

2 | GEOLOGICAL BACKGROUND

2.1 | The Daye ore district

The Daye ore district, which is located in the westernmost part of the MLYRB (Figure 1a), hosts one of the largest concentrations of Cu–Fe–Au skarn deposits in China and additional porphyry Cu–Mo–(W) deposits (Pan & Dong, 1999; Zhai et al., 1996). The basement is dominated by Cambrian to Middle Triassic marine carbonates, clastic rocks and flysch-type successions with a total thickness of over 6 km. Late Triassic to Middle Jurassic terrigenous clastics and early Cretaceous volcanic and sedimentary rocks outcrop locally (Figure 1b; Shu et al., 1992). The sedimentary rocks which host mineralization in the Daye ore district are mainly of the Lower to Middle Triassic Daye and Jialingjiang Formation (Pan & Dong, 1999; Shu et al., 1992). These were subject to Indosinian deformation in the Cambrian to Middle Triassic which produced a series of WNW- to NW-trending folds and numerous NNE faults. The folds and faults were a major control on the emplacement of igneous intrusions and development of mineralization (Shu et al., 1992).

Magmatic rocks in the Daye ore district are dominated by six plutons which are, from north to south, the Echeng, Tieshan, Jinshandian, Lingxiang, Yangxin, and Yinzu (Figure 1b). In addition, there are nearly 150 small quartz diorite, granodiorite and granite porphyry stocks occurring in or around the major plutons, such as the Tongshankou and Tonglushan (Liu et al., 2009). These major plutons and stocks formed between ca. 152 and 127 Ma (e.g., Chu et al., 2020; Li et al., 2009; Xie, Mao, & Zhao, 2011). According to Xie et al. (2013), the deposits and their associated igneous rocks in the Daye ore district can be divided into: (1) 144–137 Ma porphyry–skarn-style Cu–Mo–(W) and skarn-style Cu–Fe–Au–Mo–W deposits associated with intermediate to felsic porphyritic stocks (Suite 1;

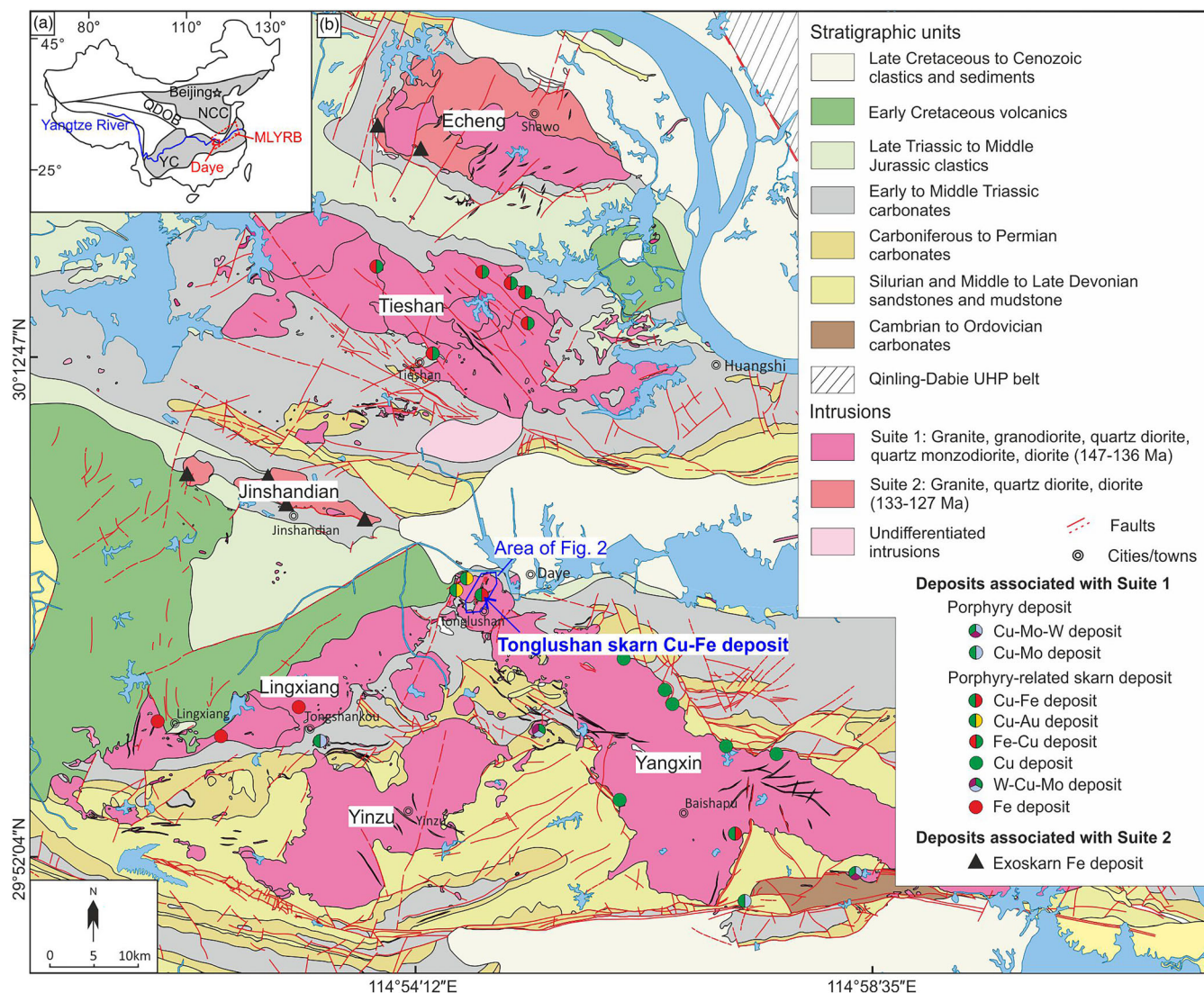


FIGURE 1 (a) Schematic map of China showing the location of the Middle-Lower Yangtze River metallogenic belt (MLYRB) and the Daye ore district (modified after Li et al., 2014). (b) Simplified geological map of the Daye ore district showing the main stratigraphic units, intrusions and mineral deposits (modified after maps provided by the Hubei Geological Bureau First Geological Brigade). NCC, North China Craton; QDOB, Qinling-Dabieshan Orogenic Belt; YC, Yangtze Craton. Area outlined in blue shows the location of the map in Figure 2.

Figure 1b); and (2) 133–120 Ma skarn-style Fe deposits related to similar age granitoids (Suite 2; Figure 1b).

2.2 | Tonglushan Cu–Fe deposit

The Tonglushan Cu–Fe deposit (30°04′30″ N, 114°55′42″ E) lies around 3 km SW of Daye city, in the central Daye ore district (Figure 1b). It is comprised of massive auriferous Fe-oxides and Cu–Fe-sulphides and has proven reserves of 1.08 Mt Cu (1.78% Cu), 60 Mt Fe (41.1% Fe), 70 t Au (0.38 g/t) and 508 t Ag (Shu et al., 1992; Zhang, Chu, et al., 2020). The deposit is centered on the Tonglushan QMD stock which was emplaced between 141 and 139 Ma (zircon U–Pb; Zhang et al., 2021) mainly

into Lower Triassic (dolomitic) limestones of the Daye Formation (Figure 2).

2.2.1 | Igneous precursors and endoskarns

The Tonglushan QMD porphyry has a high-K calc-alkaline and I-type affinity. It is thought to have been derived by partial melting of enriched lithospheric mantle and subsequent 5–20 wt.% assimilation of continental crust components (Li et al., 2009; Xie, Mao, & Zhao, 2011). The mineralogy of the porphyry is dominated by plagioclase (50%–55%), quartz (10%–15%), hornblende (10%–15%), K-feldspar (5%–10%), with lesser biotite (<2%), most of which occurs as both phenocryst and groundmass

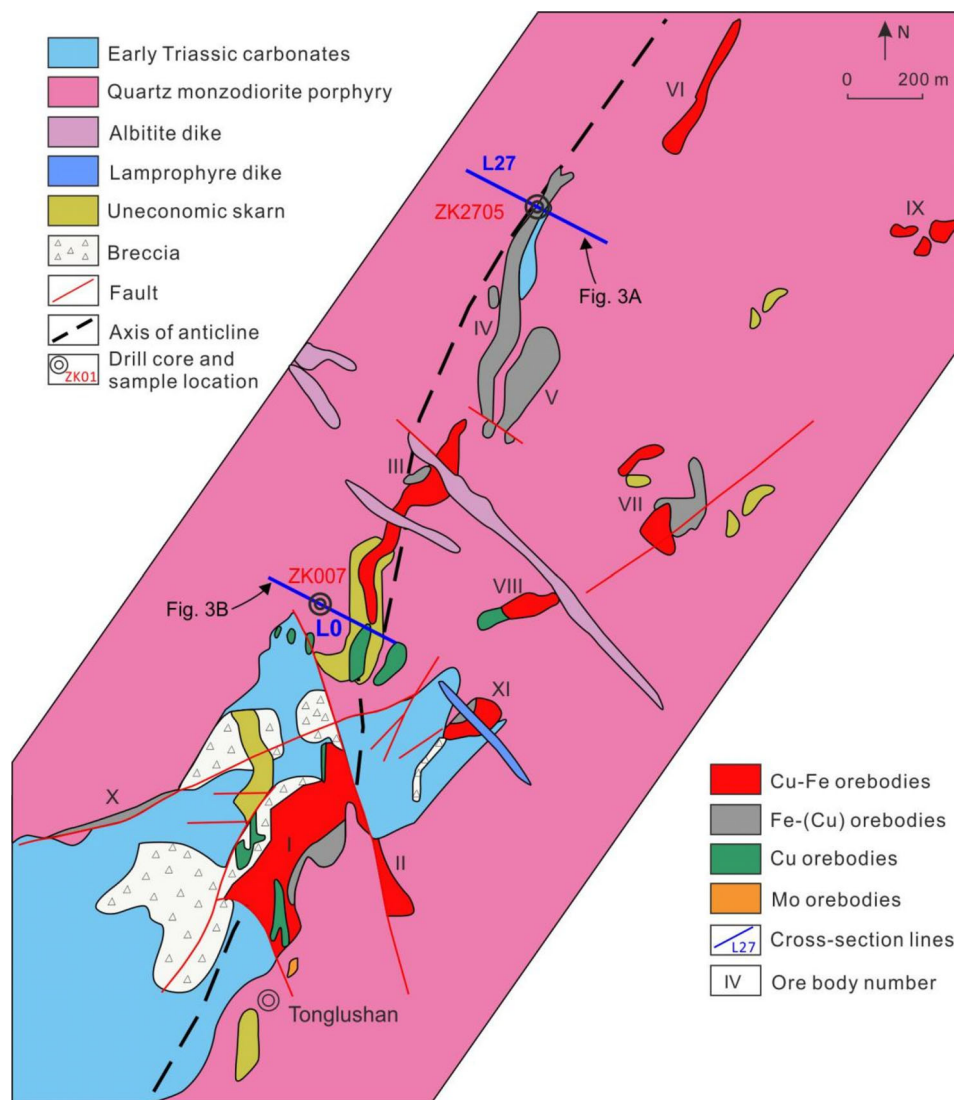


FIGURE 2 Simplified geological map of the Tonglushan Cu–Fe deposit, showing the distribution of the main exposed Cu–Fe orebodies. Note the hydrothermal breccias in the SW part of the area (modified after the maps provided by the Hubei Geological Bureau First Geological Brigade). Blue lines show the locations of the cross-sections in Figure 3.

phases (Zhang et al., 2018; Zhang et al., 2021). Accessory minerals, which make up around 3%–4% of the samples, are mainly apatite, magnetite and titanite (Duan & Jiang, 2017). The QMD has undergone varying degrees of potassic and sodic alteration, carbonatization and endoskarn formation (Shu et al., 1992; Zhao et al., 2012).

The characteristics of potassic and sodic alteration and the endoskarns are detailed in Zhang, Williamson, Rollinson, et al. (2023); we briefly summarize these below:

1. Potassic and sodic alteration in the Tonglushan QMD porphyry are widely distributed but their intensity is weak, with original igneous textures and primary mineral relicts preserved. The potassic alteration is characterized by the development of K-feldspar-biotite quartz veins, and the replacement of plagioclase and hornblende by K-feldspar and biotite, respectively, and weak Cu–Fe sulphide mineralization. Sodic alteration is characterized by albitite-calcite veins crosscutting earlier K-silicate-quartz veins, and the replacement of plagioclase and K-feldspar

by albite, chlorite and calcite, and amphibole and biotite by calcite, chlorite, and titanite.

2. Endoskarn occurs as <100 m wide zones within the QMD stock and up to its contacts with carbonate host rocks and xenoliths. The endoskarns in the Tonglushan QMD formed as a result of six paragenetically distinct stages of alteration: (1) muscovite-dominated (muscovite); (2) prograde skarnification (e.g., garnet, diopside, and calcic plagioclase); (3) retrograde skarnification (e.g., epidote, allanite, and calcite); (4) potassic alteration (e.g., K-feldspar and biotite); (5) sodic alteration (e.g., sodic plagioclase and calcite); and (6) carbonate veins and replacements.
3. Towards the margins of the QMD stock, the intensity of endoskarn alteration generally increases; igneous textures are almost completely overprinted by prograde garnet-dominated assemblages proximal to the contacts with country rocks and xenoliths. The massive garnet skarn, which generally formed within 30 m of the contact with carbonate rocks, is mainly composed of pale

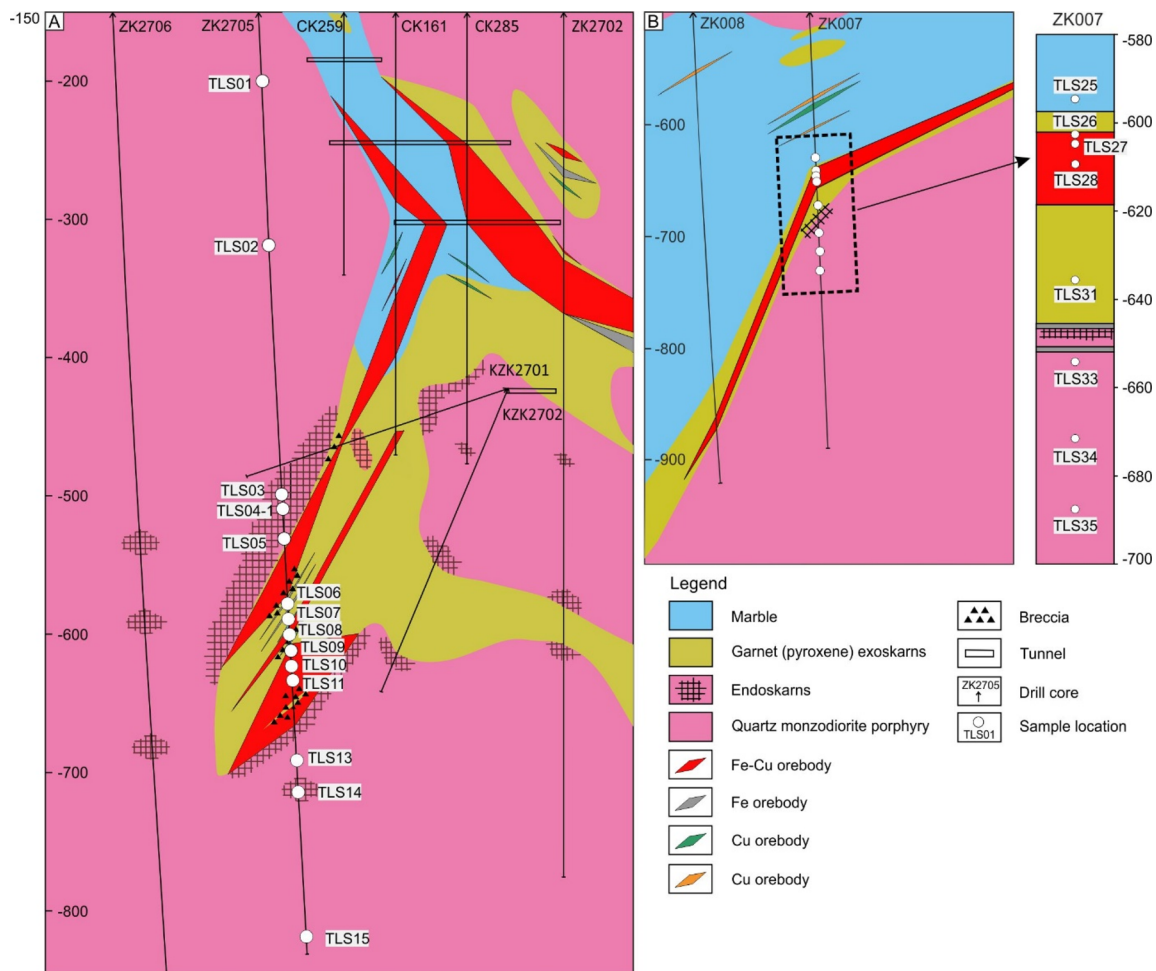


FIGURE 3 Cross-sections (a) L27 and (b) L0 in the Tonglushan Cu–Fe deposit (see lines of sections on Figure 2) showing endoskarns, different types of ore bodies and sample locations (modified after maps provided by the Hubei Geological Bureau First Geological Brigade).

brown, medium- to coarse-grained and euhedral to subhedral garnet. The garnet veins and garnet-diopside-plagioclase endoskarn formed further within the stock. The garnet veins have variable widths ranging from a few mm to several cm. The garnet-diopside-plagioclase endoskarn is characterized by the replacement of QMD with granditic garnet, diopside and plagioclase. The diopside endoskarn occurs only locally and furthest within the QMD. It is dark green in color as almost all mafic minerals have been converted to diopside. Diopside also occurs in veins (1–2 mm wide) crosscutting the rock.

2.2.2 | Carbonate protoliths and exoskarns

The (dolomitic) limestones of the Daye Formation, which are the wall rocks of the QMD pluton and occur as xenoliths (incorporated fragments) within the QMD, were the main protoliths for exoskarn development and Cu-Fe

mineralization (Li et al., 2010; Shu et al., 1992; Xie, Mao, Zhao, Wei, et al., 2011). These carbonates were metamorphosed to marble and dolomitic marble within a few hundred meters of the contact with the QMD stock (Zhao et al., 1990). Two distinct types of exoskarn have been recognized which are thought to have had different carbonate protoliths: (1) diopside-phlogopite-actinolite exoskarns formed from dolomitic marble; and (2) garnet-epidote exoskarns formed from calcite-dominated marble (Zhao et al., 2012). Four stages of alteration and mineralization affected the carbonates: (1) prograde skarnification; (2) retrograde skarnification (Fe mineralization); (3) quartz-sulfide (Cu, Au) mineralization; and (4) carbonate veins and replacements (Zhao et al., 1990; Zhao et al., 2012). In general, Cu–Fe orebodies are located proximal to the QMD stock whereas Cu–(Au) and Mo orebodies occur within the exoskarn, further away from the pluton (Figure 2).

From the cross-sections L27 and L0 in Figure 3 (lines of sections in Figure 2), the marble xenoliths drilled

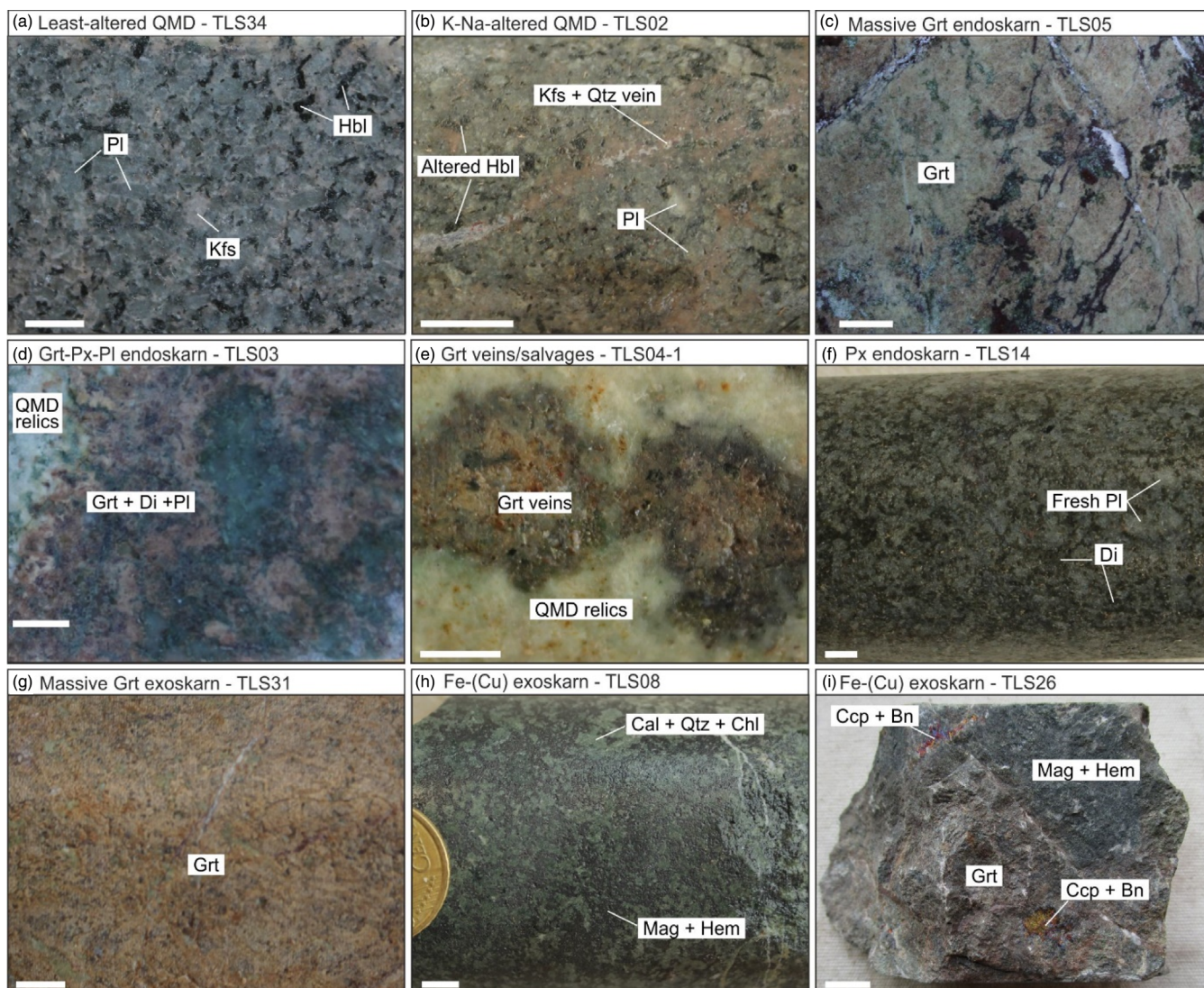


FIGURE 4 Photographs of representative least- and potassic-sodic-altered quartz QMD, endoskarns and exoskarns from the Tonglushan system. (a) Characteristic mineralogy and porphyritic texture of relatively fresh QMD. (b) Kfs + Bt + Qtz veins in potassic-sodic-altered QMD. (c) Massive Grt endoskarn, no igneous textures remain. (d) Grt-Di-Pl endoskarn, QMD relics remain. (e) Grt veins/salvages, QMD relics remain. (f) Di endoskarn, relatively fresh Pl phenocrysts remain. (g) Massive Grt exoskarn. (h) Grt exoskarn replaced by Mag + Hem and Cal + Qtz + Chl assemblages. (i) Grt exoskarn replaced by Mag + Hem, then cut and overprinted by Ccp + Bn. The length of the scale bar is 0.5 cm. Bn, bornite; Bt, biotite; Cal, calcite; Ccp, chalcopryrite; Chl, chlorite; Di, diopside; Grt, garnet; Hbl, hornblende; Hem, hematite; Kfs, K-feldspar; Mag, magnetite; Pl, plagioclase; Qtz, quartz. Mineral abbreviations within this paper follow the guidelines set out by Warr (2021).

were dominantly metasomatised to garnet exoskarns. These occasionally contain clinopyroxene-rich layers and lenses seen in drill cores ZK2705 and ZK007 (Figure 3a, b). Three generations of garnet have been recognized (Zhang et al., 2019; Zhao et al., 2012): Grt1 ($Ad_{>84}$) and Grt2 ($Ad_{18-100}Gr_{0-80}$), which generally occur in massive garnet exoskarns closely related to Fe—Cu mineralization, and Grt3 ($Ad_{18-100}Gr_{0-80}$) in poorly mineralized cm-scale veins. All garnet exoskarns display variable intensities of retrograde alteration manifested as overprinting chlorite \pm calcite \pm quartz \pm phlogopite \pm amphibole,

which are associated with Fe mineralization. Copper mineralization was produced during a later quartz-sulphide stage (Zhao et al., 2012).

3 | MATERIALS AND METHODS

3.1 | Samples

Twenty-two samples from two drill cores (ZK2705 and ZK007; Figure 3) through the Tonglushan deposit were

analyzed in this study; the samples were provided by the Hubei Geological Bureau First Geological Brigade. These samples were selected as being visually representative of the QMD protolith and as many of the different alteration styles as possible. Those chosen include two relatively fresh QMD (Figure 4a), five weakly potassic-sodic-altered QMD (Figure 4b), four endoskarns (Figure 4c–f), three garnet exoskarns (Figure 4g), seven Fe–(Cu) exoskarn ores (Figure 4h, i), and one from a carbonate xenolith. Details of sample locations and descriptions, including rock types, key minerals, styles of alteration and observed veins/veinlets, are provided in the Electronic Supplementary Materials (ESM_Supplementary Table 1).

3.2 | Whole-rock geochemical analysis

Three to 5 cm lengths of 7 cm diameter drill core were jaw crushed to a 5–10 mm particle size and then ground in a tungsten carbide Tema mill to obtain rock powder of less than 200 mesh. The crusher and Tema were thoroughly cleaned with methylated spirits between each sample to reduce the potential for cross-contamination.

Sample powders (100 mg) were placed into 50 mL Teflon digestion vessels and then dissolved in 4 mL of distilled HF and 4 mL HNO₃ + 3HCl at 160°C for at least 8 h. The solutions were subsequently taken to dryness and the residues then digested in 1 mL of HClO₄, and then again taken to dryness. Once cool, 1 mL of HNO₃ was added to each vessel and this heated to 180°C until dry. The residue was then digested in 1 mL of concentrated HNO₃ and 5 mL of deionized H₂O and held at 100°C in an oven for 30 min. Once allowed to cool, 44 mL of deionized H₂O was added to each vessel, mixed in and the solution then transferred to a 50 mL polypropylene sample container. Five milliliter of each sample solution was diluted with 45 mL of 5% HNO₃ in a sealed polypropylene sample tube (QMx Digiprep) ready for analysis.

Trace element (rare earth elements (REE), V, Cu, Zn, Rb, Sr, Y, Sc, Zr, Nb, Mo, Sn, Sb, Cs, Ba, Hf, Ta, W, Pb, Th, and U) and some major element (Fe, Mn) concentrations were determined using an Agilent 7700 quadrupole mass spectrometer (ICP-MS) at Camborne School of Mines, University of Exeter. Detection limits were better than 1 ppb for all elements except Fe and Zn (1–1.5 ppb) (ESM_Supplementary Table 2). Procedural blank contributions were negligible.

Pairs of certified reference materials (CRM: AGV-2 (Guano Valley Andesite) and DNC-1 (North Carolina Diabase)) were analyzed at the beginning and end of sessions to determine experimental accuracy and precision.

For AGV-2, the accuracy was better than 1% for Fe, Cu, Sr, La and Nd, 1%–5% for Sc, V, Mn, Zr, Nb, Cs, Ce, Pr, Sm, Eu, Dy, Er, Tm, Yb, and Lu, 5%–10% for Rb, Y, Ba, Ho, Hf and Pb, 10%–15% for Sn, Th and U, and > 20% for Zn, Sb and Ta. For DNC-1, the accuracy was better than 1% for Fe, Cu, Nd and Yb, 1 to 5% for Sc, Y, Zr, Sb, Ba, Eu, Gd, Dy and Ho, 5 to 10% for V, Mn, Sr, and Pb, 10%–15% for Rb and La, and > 20% for Zn and Nb. Precision (2σ , $n = 9$) was better than 20% for most elements except Zn, Mo, Sn, Sb, Ta, and W. Analytical accuracy and precision for different elements are summarized in ESM_Supplementary Table 3.

Major elements (Al, Fe, Mn, Mg, Na, K, Ca, Ti, P, and S) were determined using an Agilent 5110 ICP-OES at Camborne School of Mines, University of Exeter. Si could not be determined as it is lost to the vapor phase when using HF in sample dissolution. The same sample solutions used for ICP-MS were diluted by a further 10× to give a 1:500 ratio of sample solution to 5% HNO₃. Due to the wide range of element concentrations in the solutions, polynomial regressions were applied to fix most of the matrix effects. Detection limits were 0.002 wt % for Fe₂O₃, 0.012 wt % for Al₂O₃, 0.022 wt % for MgO, 0.004 wt % for CaO, 0.001 wt % for Na₂O, 0.002 wt % for K₂O, 0.002 wt % for TiO₂, 0.0001 wt % for MnO, 0.095 wt % for P₂O₅. Based on repeated analyses of AGV-2, analytical accuracy was better than 5% for Fe₂O₃, CaO, Na₂O, TiO₂, and P₂O₅, and 5%–8% for Al₂O₃, MgO, and K₂O. For DNC-1, accuracy was better than 8%, except for K₂O and P₂O₅ (better than 23%), and precision (2σ , $n = 9$) was better than 5%, except for K₂O (14%). Data for analytical accuracy and precision using ICP-OES are shown in ESM_Supplementary Table 4.

As an additional check, concentrations of Fe and Mn in the samples were determined using both ICP-MS and ICP-OES; the results were in good agreement, see Figure 5.

3.3 | Isocon analysis

Bulk mass changes and net element transfers during the formation of exoskarn, endoskarn and weak potassic-sodic alteration in the QMD were quantified using isocon analysis (Grant, 1986; Gresens, 1967). This involves “plotting element concentrations in an altered sample (or mean of a group of altered samples) against a least-altered reference protolith”. Immobile elements plot on a no relative gain or loss of mass “isocon” line which passes through the origin on an X–Y plot as infinite dilution ultimately decreases the immobile element concentration to zero (Cail & Cline, 2001; Finlow-Bates &

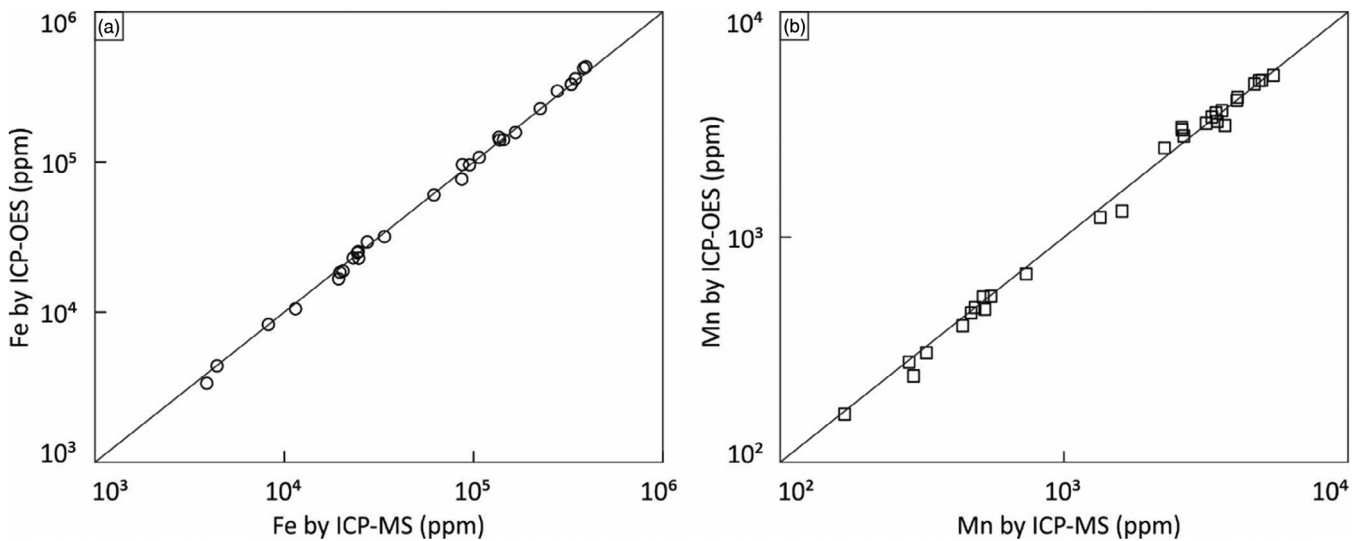


FIGURE 5 Values determined for Fe and Mn in whole-rock samples by ICP-MS compared with ICP-OES. There is good agreement between methods.

Stumpfl, 1981). The isocon was derived using the equation of Grant (1986):

$$C^A = (M^O/M^A) * C^O.$$

where C^A and C^O are concentrations of components in the altered and least-altered rocks, respectively. M^A and M^O represent mass of altered and least-altered rocks, respectively. Grant (1986) states that the most useful measure of gains and losses of mobile components is the change in concentration of a component (ΔC_i) relative to its concentration prior to alteration (C_i^O), given by the equation:

$$\Delta C_i/C_i^O = (M^A/M^O) * (C_i^A/C_i^O) - 1.$$

in which i represents a mobile constituent. As M^O/M^A represents the slope of the isocon, the above equation can be written as:

$$\Delta C_i/C_i^O = (1/\text{slope}) * (C_i^A/C_i^O) - 1.$$

Mass changes (ΔM) can be obtained by:

$$\Delta M = (M^A/M^O) - 1.$$

The slope of the isocon relates to the net mass change during alteration: a slope >1 indicates bulk mass loss (e.g., by net mineral dissolution) and a slope <1 indicates

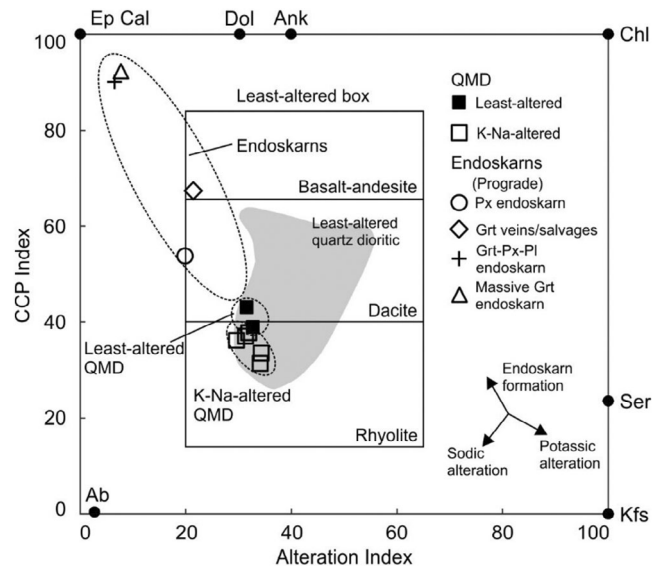


FIGURE 6 Alteration Box Plot diagram of Large et al. (2001) with data added for endoskarns and least- and potassic-sodic-altered QMD from the Tonglushan Cu-Fe deposit. CCP index (chlorite-carbonate-pyrite index) = $100(\text{MgO} + \text{FeO})/(\text{MgO} + \text{FeO} + \text{Na}_2\text{O} + \text{K}_2\text{O})$, Alteration index (Ishikawa's Alteration Index; Ishikawa et al., 1976) = $100(\text{K}_2\text{O} + \text{MgO})/(\text{K}_2\text{O} + \text{MgO} + \text{Na}_2\text{O} + \text{CaO})$. Ab, albite; Ank, ankerite; Cal, calcite; Chl, chlorite; Dol, dolomite; Di, diopside; Ep, epidote; Grt, garnet; Kfs, K-feldspar; Pl, plagioclase; Ser, sericite.

bulk mass gain (e.g., by mineral precipitation). Components that lie above the isocon have been added, whereas those below have been lost due to alteration. A scaling factor is used to allow all elements (which may show a very wide range of concentrations) to be plotted on the same diagram.

TABLE 1 Whole-rock geochemistry of least- and K–Na-altered QMD and endoskarns in the Tonglushan system.

Element/ sample	QMD							Endoskarns				
	Least- altered TLS13	K–Na-altered						Di TLS14	Grt veins/ salvages TLS04-1	Grt- Di-Pl TLS03	Massive Grt TLS05	
		TLS34	TLS01	TLS02	TLS15	TLS33	TLS35					
Al ₂ O ₃	15.3	15.5	14.6	14.9	15.7	14.3	15.7	16.7	19.1	12.8	10.2	
Fe ₂ O ₃	4.21	3.63	3.29	2.70	3.57	3.28	2.64	4.56	2.38	13.8	15.4	
MgO	1.36	1.32	1.21	1.31	0.92	1.07	1.01	2.39	3.48	0.89	0.64	
CaO	5.19	4.74	5.01	5.06	5.64	4.90	4.54	7.31	10.4	24.6	25.0	
TiO ₂	0.57	0.52	0.55	0.53	0.55	0.50	0.49	0.60	0.54	0.50	0.50	
P ₂ O ₅	0.26	0.25	0.26	0.27	0.26	0.23	0.24	0.29	0.26	0.18	0.23	
MnO	0.07	0.06	0.06	0.05	0.07	0.06	0.04	0.09	0.17	0.47	0.67	
Na ₂ O	4.36	4.56	4.27	4.39	4.61	4.27	4.37	5.24	2.51	0.74	0.07	
K ₂ O	3.00	3.17	3.15	3.62	3.38	3.13	3.59	0.72	3.24	0.87	1.40	
S	0.24	q.l.	0.30	0.20	q.l.	q.l.	q.l.	0.11	0.13	0.21	0.12	
Ba	876	1128	835	863	883	916	871	198	237	12.1	8.71	
Rb	74.3	66.9	72.7	65.4	57.0	53.3	54.3	5.12	72.4	43.0	96.4	
Sr	1044	1140	935	945	981	894	884	1346	1846	160	113	
Y	16.4	15.5	15.2	15.0	16.6	15.2	14.4	16.6	14.8	15.4	18.1	
Sb	0.07	0.06	0.12	0.12	0.08	0.08	0.07	0.09	0.73	0.20	0.56	
Cs	0.92	0.83	1.39	0.73	0.51	2.09	0.90	0.24	11.7	10.2	29.4	
Nb	18.6	18.1	18.7	17.7	18.9	17.2	17.4	17.9	25.2	24.8	7.37	
Sn	1.28	1.12	1.36	1.29	1.24	1.20	1.15	1.43	1.70	6.63	10.0	
Sc	6.93	6.38	6.67	6.58	6.36	6.11	5.98	7.01	5.58	5.73	6.97	
V	78.7	70.8	68.6	74.5	64.7	70.9	54.6	81.0	22.8	83.6	73.8	
Zr	24.9	40.2	32.9	29.6	31.0	35.2	28.3	30.3	37.8	111	157	
Hf	1.05	1.40	1.32	1.28	1.19	1.36	1.14	1.19	1.42	2.84	3.83	
Pb	7.25	10.1	13.7	8.89	6.32	8.08	6.20	5.77	10.4	5.09	5.20	
Th	10.4	7.81	11.4	9.81	6.60	9.62	9.20	7.51	14.2	10.7	9.03	
U	2.05	1.66	2.30	2.06	1.23	1.51	1.33	2.17	1.66	3.54	7.25	
Cu	3.82	18.6	157	84.5	2.81	113	5.05	5.62	20.9	15.1	11.	
Zn	33.7	44.3	24.3	18.6	30.6	56.3	35.8	41.4	64.9	18.7	19.2	
Mo	1.59	1.14	4.57	3.38	1.19	1.02	1.26	1.73	2.41	9.72	2.50	
La	51.4	47.2	49.4	48.7	45.6	43.1	41.4	56.6	43.1	24.6	110	
Ce	87.8	77.8	75.7	79.0	76.8	69.6	64.8	106	80.8	55.7	128	
Pr	10.8	10.0	10.2	10.3	10.1	8.90	9.04	12.2	9.89	6.58	10.2	
Nd	39.1	36.3	36.9	36.4	36.4	32.4	32.1	42.8	35.6	26.6	35.1	
Sm	6.91	6.35	6.51	6.23	6.47	5.53	5.75	7.22	6.30	5.42	6.87	
Eu	1.78	1.70	1.64	1.67	1.62	1.48	1.45	1.77	1.36	1.38	1.87	
Gd	4.98	4.56	4.76	4.48	4.76	4.21	4.14	5.28	4.47	4.31	5.41	
Tb	0.57	0.53	0.55	0.53	0.55	0.50	0.47	0.60	0.53	0.50	0.61	
Dy	3.38	2.95	3.10	3.04	3.17	2.96	2.87	3.48	2.95	3.06	3.74	
Ho	0.58	0.54	0.56	0.53	0.57	0.53	0.50	0.60	0.52	0.53	0.66	
Er	1.66	1.53	1.48	1.53	1.64	1.49	1.44	1.69	1.43	1.55	1.86	
Tm	0.21	0.20	0.19	0.19	0.21	0.19	0.19	0.21	0.18	0.20	0.25	

(Continues)

TABLE 1 (Continued)

Element/ sample	QMD							Endoskarns			
	Least- altered TLS13	K–Na-altered						Di TLS14	Grt veins/ salvages TLS04-1	Grt- Di-Pl TLS03	Massive Grt TLS05
		TLS34	TLS01	TLS02	TLS15	TLS33	TLS35				
Yb	1.40	1.36	1.36	1.33	1.38	1.30	1.26	1.44	1.30	1.38	1.65
Lu	0.19	0.17	0.17	0.17	0.19	0.18	0.17	0.19	0.16	0.18	0.22

Abbreviations: Di, diopside; Grt, garnet; Pl, plagioclase.

4 | RESULTS

4.1 | Least-altered precursors

Using unaltered samples for mass balance calculations would be preferable, however identifying such rocks in a widely altered magmatic-hydrothermal province is difficult (Grant, 2005). In the Tonglushan system, least-altered precursors were selected on the basis of containing the lowest proportion of alteration minerals, as determined from petrographic analysis. For Isocon analysis of the endoskarns, samples TLS13 and TLS34 were chosen as the least-altered representatives of the QMD protolith, although these samples showed evidence of minor alteration of plagioclase to K-feldspar + albite, and hornblende to chlorite + calcite (ESM_Supplementary Table 1). For isocon analysis of the exoskarns, sample TLS25 was the most representative of the carbonate protolith, despite containing rare narrow chlorite veinlets.

The extent of alteration in the QMD was assessed by plotting all sample whole-rock data on the Alteration Box Plot diagram of Large et al. (2001) in Figure 6. Although the Alteration Box Plot was originally designed to assess the types and levels of alteration in volcanics associated with volcanic-hosted massive sulphide deposits, it has also been used for porphyry rocks, most notably by Ahmed et al. (2019) and Zhang, Tian, et al. (2020). Samples of QMD selected as being least-altered (TLS13 and TLS34) plot within the least-altered box of the diagram, whereas weakly potassic-sodic-altered QMD and endoskarns lie on a trend towards K-feldspar and epidote/calcite enrichment, respectively.

4.2 | Geochemical composition of main lithologies

Major and trace element geochemical data for the least-altered and weakly potassic-sodic-altered QMD, endoskarns, exoskarns and marble from the Tonglushan system are listed in Tables 1 and 2.

Compared with the least-altered QMD (TLS13 and TLS34), potassic-sodic-altered rocks contain similar contents of Al_2O_3 , CaO, TiO_2 , P_2O_5 , MnO, Ba, Sn, V, high field strength elements (HFSE) (e.g., Zr and Hf) and REE, but have lower Fe_2O_3 (2.6–3.6 vs. 3.6–4.2 wt %), MgO (0.92–1.3 vs. 1.3–1.4 wt %) and Sr (884–981 vs. 1044–1140 ppm) and higher K_2O (3.1–3.6 vs. 3.0–3.2 wt %) and Cu (2.8–157 vs. 3.8–18.6 ppm) (Table 1). The endoskarns have similar contents of TiO_2 , P_2O_5 and REE (except La and Ce) compared with the least-altered or potassic-sodic-altered QMD, much higher CaO (7.3–25.0 wt %), Fe_2O_3 (4.6–15.4 wt %), MnO (0.09–0.67 wt %), Sn (1.4–10.0 ppm), Zr (30.3–157 ppm), Hf (1.2–3.8 ppm) and U (1.7–7.3 ppm), and variable contents of Al_2O_3 (10.2–19.1 wt %), MgO (0.64–3.5 wt %), Na_2O (0.07–5.24 wt %), K_2O (0.65–3.24 wt %), Rb (5.12–96.35 ppm) and Sr (113–1846 ppm). Amongst the endoskarns, the massive garnet variety contains the highest concentrations of Fe_2O_3 , CaO, MnO, Rb, Zr, Hf, La, Ce, and heavy REE.

The marble contains the highest concentration of CaO, and low concentrations of Al_2O_3 , Fe_2O_3 , MgO, MnO, TiO_2 , Na_2O , K_2O , P_2O_5 , and REE (Table 2). The massive garnet exoskarns and Fe–(Cu) exoskarns have similar ranges of Al_2O_3 (1.1–7.6 wt %), MgO (0.20–3.1 wt %), MnO (0.32–0.64 wt %), Na_2O (0.03–0.07 wt %) and K_2O (<1.1 wt %). The Fe–(Cu) exoskarns have significantly higher Fe_2O_3 (up to 61.8 wt %) and Cu (up to 7497 ppm) concentrations and lower CaO and REE contents compared with the massive garnet exoskarns.

4.3 | Immobile elements during alteration

By plotting the concentration of one element versus another, that is, using the method of Cail and Cline (2001), titanium was identified as having been “immobile” (or at least to show minimum mobility) in the formation of all samples collected. It was therefore used to define isocons and to quantify mass changes and element mobility due to potassic-sodic alteration and in the formation of endoskarns

TABLE 2 Whole-rock geochemistry of marble, garnet exoskarns and Fe–(Cu) exoskarn ores in the Tonglushan system.

Element/sample	Exoskarns										
	Marble	Massive Grt				Fe–(Cu) ores					
		TLS25	TLS06	TLS07	TLS31	TLS08	TLS09	TLS10	TLS11	TLS26	TLS27
Al ₂ O ₃	0.96	4.08	4.75	7.62	2.07	2.03	1.05	2.04	4.34	5.02	6.18
Fe ₂ O ₃	0.48	20.1	21.0	20.2	60.4	51.4	61.8	32.5	42.5	47.0	47.1
MgO	0.35	2.49	0.67	3.08	0.48	0.21	0.20	0.51	0.87	1.03	1.25
CaO	45.4	26.7	27.7	26.1	15.0	12.6	10.9	19.8	15.3	14.9	12.3
TiO ₂	0.04	0.34	0.35	0.38	0.20	0.15	0.05	0.09	0.18	0.20	0.37
P ₂ O ₅	q.l.	0.09	0.04	0.06	q.l.	q.l.	q.l.	q.l.	0.04	q.l.	q.l.
MnO	0.03	0.41	0.53	0.52	0.38	0.32	0.39	0.45	0.44	0.64	0.63
Na ₂ O	0.06	0.05	0.04	0.06	0.06	0.07	0.06	0.07	0.03	0.06	0.06
K ₂ O	0.08	0.01	0.31	0.07	0.03	0.03	q.l.	q.l.	0.28	1.09	0.20
S	0.20	0.25	0.16	q.l.	0.29	0.15	0.29	0.33	0.21	0.09	0.10
Ba	21.1	41.4	7.22	11.4	2.96	6.69	2.51	4.23	23.6	10.7	7.60
Rb	9.42	3.88	25.5	6.39	3.52	2.77	0.51	0.54	26.3	109	33.2
Sr	2902	85.0	101	72.4	1167	97.5	80.4	128	129	135	127
Y	3.17	17.3	12.7	16.5	3.62	19.7	7.83	18.2	8.16	7.66	11.5
Sb	0.93	0.24	0.31	0.13	0.30	0.63	0.22	0.32	6.70	1.55	2.45
Cs	1.29	0.59	3.23	0.44	0.31	0.87	0.22	0.16	8.03	17.4	19.3
Nb	0.97	4.38	5.41	3.98	1.58	2.11	5.29	2.73	6.37	7.80	3.89
Sn	0.40	24.2	22.3	16.9	7.49	21.8	23.1	60.5	26.4	26.4	15.8
Sc	1.24	8.77	7.02	10.3	3.44	1.33	0.83	1.47	4.24	4.22	8.79
V	7.78	60.4	53.5	72.2	46.0	488	51.2	98.8	59.3	34.4	73.2
Zr	6.23	83.4	68.1	94.3	25.2	16.8	6.45	12.9	30.4	37.3	75.0
Hf	0.13	2.41	1.86	2.64	0.77	0.45	0.21	0.42	0.88	1.15	2.22
Pb	13.2	4.02	2.28	4.90	2.57	5.49	1.55	3.93	20.2	7.76	12.5
Th	0.71	4.51	3.50	5.68	0.55	4.69	2.33	3.67	5.05	4.80	5.20
U	3.19	9.52	10.8	9.54	1.18	1.46	1.83	2.62	9.09	10.6	3.26
Cu	14.9	1214	78.2	53.7	153	621	5098	7497	2498	257	588
Zn	29.2	27.0	522	62.0	197	201	286	239	352	582	405
Mo	0.59	0.88	1.11	0.90	0.87	1.80	1.96	1.00	2.22	0.89	1.42
La	3.74	8.81	10.3	9.52	6.70	35.5	12.8	40.2	14.6	12.1	10.1
Ce	7.50	48.7	52.8	49.5	15.0	69.1	40.2	109	60.8	58.2	42.3
Pr	0.87	7.55	8.74	6.51	1.76	7.96	5.23	13.8	8.68	8.04	5.94
Nd	3.33	28.5	36.2	23.6	5.70	29.1	18.9	48.1	28.8	22.0	19.6
Sm	0.62	4.55	5.19	4.13	0.76	5.30	2.83	6.69	3.40	2.31	3.10
Eu	0.13	1.74	1.93	1.10	0.19	1.93	1.16	3.44	1.30	0.78	0.87
Gd	0.57	3.86	3.45	3.39	0.72	4.45	1.94	4.63	2.25	1.86	2.53
Tb	0.07	0.52	0.41	0.46	0.09	0.54	0.23	0.55	0.27	0.23	0.34
Dy	0.54	3.36	2.46	3.02	0.55	3.27	1.48	3.37	1.60	1.48	2.29
Ho	0.08	0.63	0.46	0.60	0.08	0.62	0.28	0.63	0.29	0.26	0.43
Er	0.30	1.86	1.31	1.84	0.25	1.74	0.85	1.90	0.87	0.83	1.31
Tm	0.02	0.24	0.17	0.25	0.01	0.20	0.11	0.25	0.10	0.10	0.18
Yb	0.26	1.68	1.22	1.72	0.21	1.24	0.87	1.71	0.73	0.73	1.25

(Continues)

TABLE 2 (Continued)

Element/sample	Exoskarns										
	Marble	Massive Grt				Fe–(Cu) ores					
		TLS25	TLS06	TLS07	TLS31	TLS08	TLS09	TLS10	TLS11	TLS26	TLS27
Lu	0.02	0.23	0.16	0.24	0.02	0.15	0.11	0.22	0.09	0.09	0.17

Abbreviation: Grt, garnet.

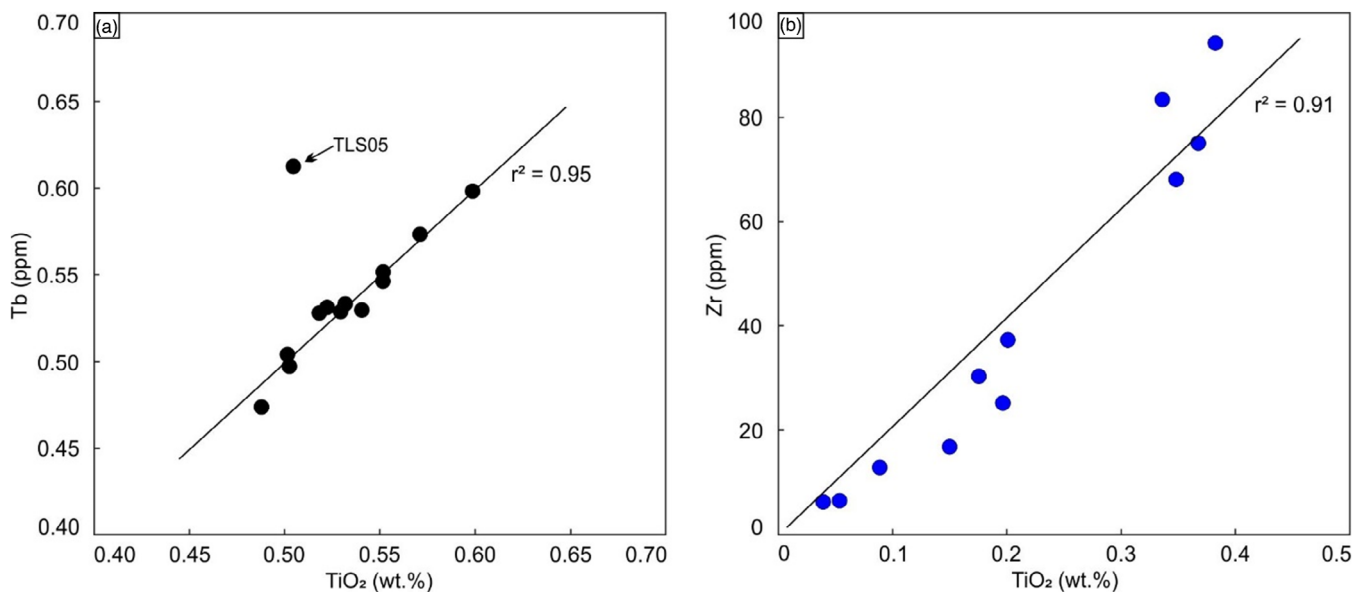


FIGURE 7 Plot of concentrations of (a) TiO₂ versus Tb in QMD and endoskarns, and (b) TiO₂ versus Zr in exoskarns. The positive correlations ($r^2 > 0.90$) suggest that TiO₂, Tb and Zr were poorly mobile during potassic-sodic alteration and endoskarn formation in the QMD and exoskarn alteration of carbonate wall rocks in the Tonglushan system. The enrichment of Tb in the massive garnet endoskarn (TLS05) could be caused by the formation of REE-rich allanite.

and exoskarns. On the diagram of TiO₂ versus Tb (Figure 7a), and TiO₂ versus Gd (not shown), there are tight linear trends (r^2 values of >0.92) that pass through the origin for samples of variously altered QMD (except TLS05; massive garnet endoskarn). These strong correlations indicate that Tb and Gd were also poorly mobile during most types of alteration of the QMD.

For the marble and garnet and Fe-(Cu) exoskarns, Sc, Zr and Hf are correlated with TiO₂ (r^2 values >0.91) indicating limited mobility during exoskarn formation (see example for Zr in Figure 7b).

4.4 | Mass changes and element transfer in the Tonglushan system

Isocon diagrams are shown in Figures 8–10 for potassic-sodic, and endoskarn alteration of the QMD and exoskarn alteration of carbonate xenoliths and wall rocks. Least-altered compositions (C^0) were the average of TLS13 and TLS34 for the QMD and TLS25 for the carbonate protolith.

4.4.1 | Potassic-sodic alteration in the QMD

The formation of potassic-sodic alteration in the QMD distal to the endoskarn (Figure 8; Table 3) involved very little mass change, as indicated from the 0.96 slope of the isocon, which suggests around 4% mass gain. Of the components considered, Al₂O₃, HFSE, Sn, V, CaO, Na₂O, Ba, Pb, and REE show little net change ($<10\%$), K₂O, Sb and Cs display various increases (14%–57% gains) and Fe₂O₃, MgO, MnO, Rb, and Sr show weak depletions (11%–18% losses). Cu and Mo were significantly added to these weakly altered rocks, for example, avg. 385% increase in Cu.

4.4.2 | Endoskarns

The formation of the massive garnet endoskarn, garnet-diopside-plagioclase endoskarn and garnet veins/salvages was associated with a mass gain of 3%–9% (Figure 9a–c). In contrast, the formation of the diopside endoskarn

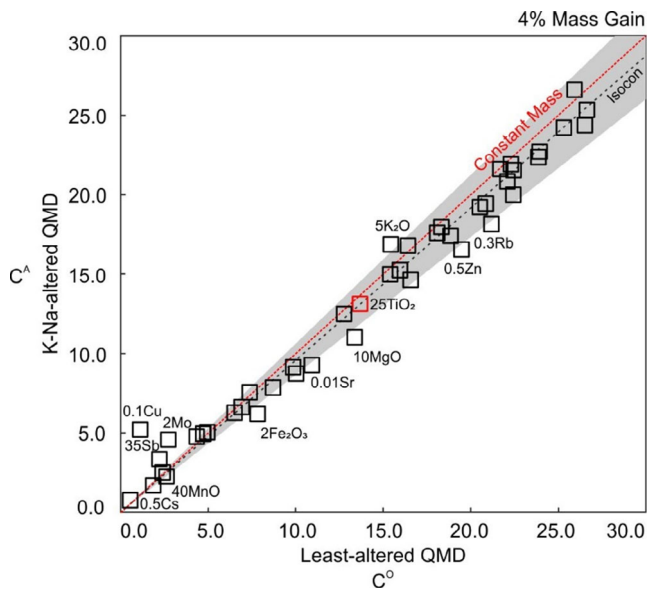


FIGURE 8 Isocon plot showing the mass change during potassic-sodic alteration in the Tonglushan QMD. The red line (1:1) represents constant mass (i.e., no change). The total mass change is indicated in the upper right corner of the plot, expressed as a percentage. TiO_2 was used as the least mobile component to define the isocon. Elements plotting within the gray-shaded area are considered ‘immobile’ (less than 10% mass change); see Table 3 for the complete list of immobile elements during alteration. The numbers before the component symbol are the scaling factors, which were used so that all components (despite their different concentrations and units) could be plotted in close proximity on the same axes. See Table 3 for element mobility and mass changes during potassic-sodic alteration.

involved a mass loss of 9% (Figure 9d). Generally, P_2O_5 shows no net change in the formation of most endoskarns (except the garnet-diopside-plagioclase endoskarn), and Sc, heavy REE (e.g., Y, Gd to Lu) remain constant, except for the TLS05 sample of massive garnet endoskarn (Figure 9; Table 3). Significant increases can be seen in some major skarn components (i.e., Fe_2O_3 , CaO, and MnO) in all endoskarns, for example, up to 326% and 445% gains in Fe_2O_3 and CaO, respectively (Figure 9; Table 3). Al_2O_3 is relatively constant in all endoskarns except in the massive garnet type where there is a depletion in Al_2O_3 of 28% (Figure 9a). For MgO, the formation of the garnet veins/salvages and diopside endoskarn involved a 126% increase whereas the massive garnet endoskarn and garnet-diopside-plagioclase endoskarn showed decreases of up to 48%. Alkalis (K_2O and Na_2O) decreased by more than 50% in the formation of all endoskarns (Figure 9a–c; Table 3) except in the diopside type which shows no net change in Na_2O (Figure 9d; Table 3). Some HFSEs appear to have been enriched as a result of the formation of the garnet-bearing endoskarns, Zr, Hf, and U by up to 422%. The light REE decrease by

up to 46% in the garnet-diopside-plagioclase endoskarn and garnet veins/salvages, whereas La and Ce increase by up to 143% in the massive garnet endoskarn (Figure 9a–c; Table 3).

4.4.3 | Massive garnet, and Fe–(Cu) exoskarns

The formation of garnet and Fe–(Cu) exoskarns involved significant overall mass losses of 78 to 89% (Figure 10). In both cases, CaO, Sr, MgO and Na_2O were strongly lost (25 to 100%; Figure 10; Table 4). K_2O showed no net change whereas it decreased significantly (81%) in the massive garnet exoskarns (Figure 10a; Table 4). There was strong addition of Fe, Cu, Mn, Sn and V in the Fe–(Cu) exoskarns, with up to a 3500% gain in Cu (Figure 10b; Table 4). The HFSE and REE were gained in the formation of the garnet and Fe–(Cu) exoskarns. For example, Zr and Hf were significantly added (up to 89%), whereas U was depleted (up to 224%) in both exoskarn types (Figure 10; Table 4).

5 | DISCUSSION

5.1 | Mobility of “immobile” elements during endoskarn formation

5.1.1 | Titanium

From the results of the Gresens’ analyses shown in Figures 8–10, Ti was the least mobile element identified in this study, as shown in many other studies of skarns (e.g., Karimzadeh Somarin, 2004; Mrozek et al., 2020). This probably indicates that the pH of the fluids responsible for alteration in the Tonglushan pluton was between 2 and 12, outside which Ti can be relatively mobile (van Baalen, 1993). The magmatic-hydrothermal fluids responsible for potassic alteration in the Tonglushan system are likely to have been only moderately acid (usually weakly acidic-to-neutral, pH of ~ 4 –5; Kouzmanov & Pokrovski, 2012), almost certainly not pH < 2. In the endoskarn-forming environment, mixing of magmatic-hydrothermal fluids with those which had interacted with the carbonate xenoliths and wall rocks would have heavily buffered their pH (Meinert et al., 2005), probably to ~ 6 –7, if such fluids were in equilibrium with calcite (Kouzmanov & Pokrovski, 2012). Overall, the pH of the fluids responsible for alteration and mineralization in the Tonglushan system was likely to have been between ~ 4 and 7, preventing the transport of Ti (Tropper & Manning, 2005).

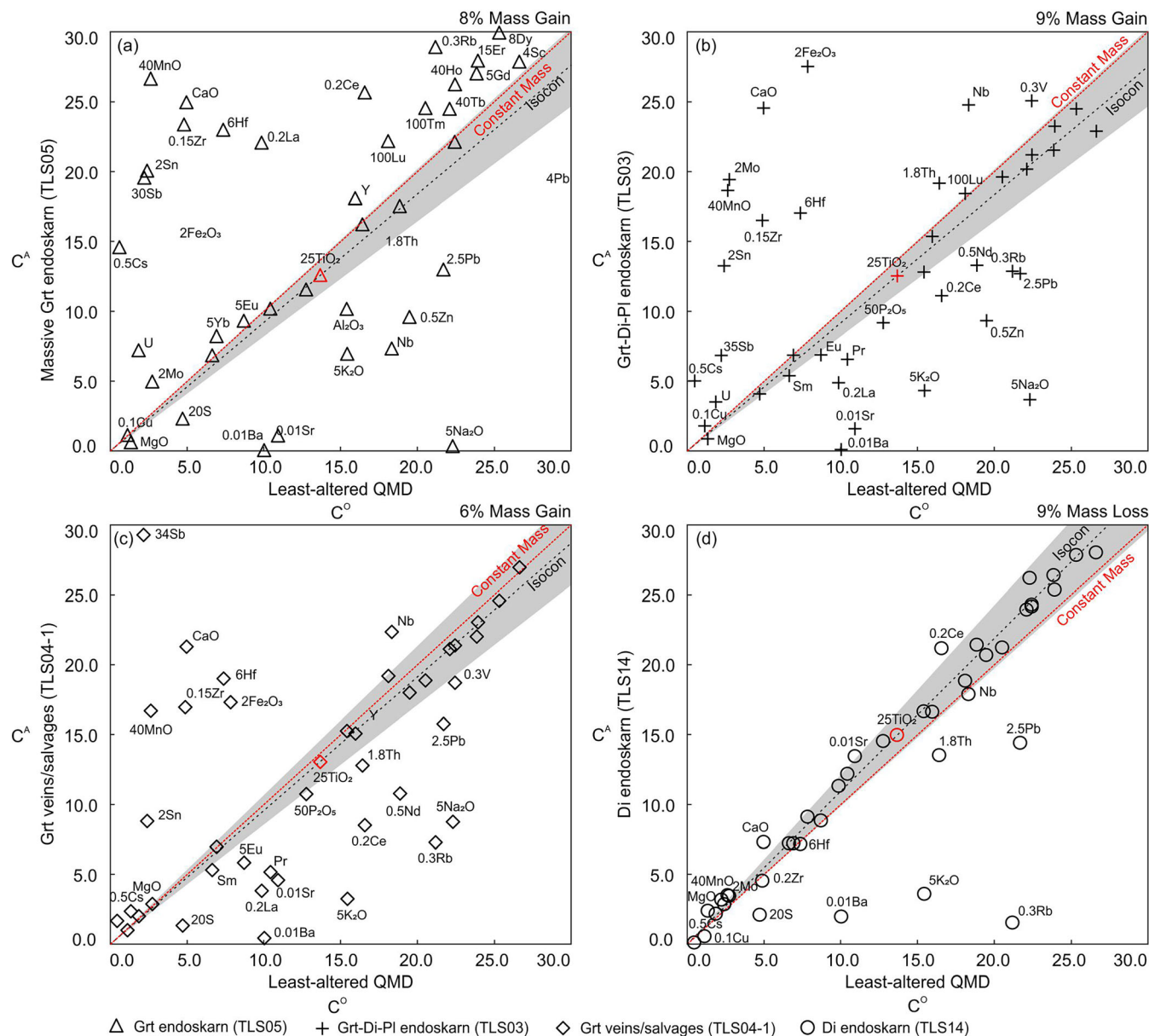


FIGURE 9 Isocon plots showing mass changes during endoskarn formation in the Tonglushan system. Element mobility and mass changes are shown for the formation of: (a) Grt endoskarn; (b) Grt-Di-Pl endoskarn; (c) Grt veins/salvages; and (d) Di endoskarn. The total mass change relative to least-altered QMD is indicated in the upper right corner of each plot, expressed as a percentage. For details related to these diagrams, see Figure 8. Di, diopside; Grt, garnet; Pl, plagioclase.

Due to the low solubility of Ti-bearing phases, Ti is unlikely to have been derived from alteration-resistant accessory minerals in the protolith, such as titanite and rutile (Angiboust & Harlov, 2017; Xiong et al., 2005). More probable, is liberation due to alteration of biotite and hornblende in the QMD, with the Ti then incorporated in-situ into skarn minerals (Mrozek et al., 2020), e.g. by replacement of garnet which in the Tonglushan garnet endoskarn contains up to 2.6 wt.% TiO₂ (Zhang et al., 2019).

5.1.2 | Aluminum

This is generally regarded as “immobile” in the formation of many skarn deposits worldwide (Karimzadeh Somarin, 2004, 2010; Lentz, 2005; Mrozek et al., 2020), but up to 28% was removed during endoskarn formation in the Tonglushan system so it must have been relatively easily transported. It is mobile in neutral and slightly acid solutions but more so in fluids which are: (1) ultra-acid (Stoffregen, 1987), which are uncommon in skarn

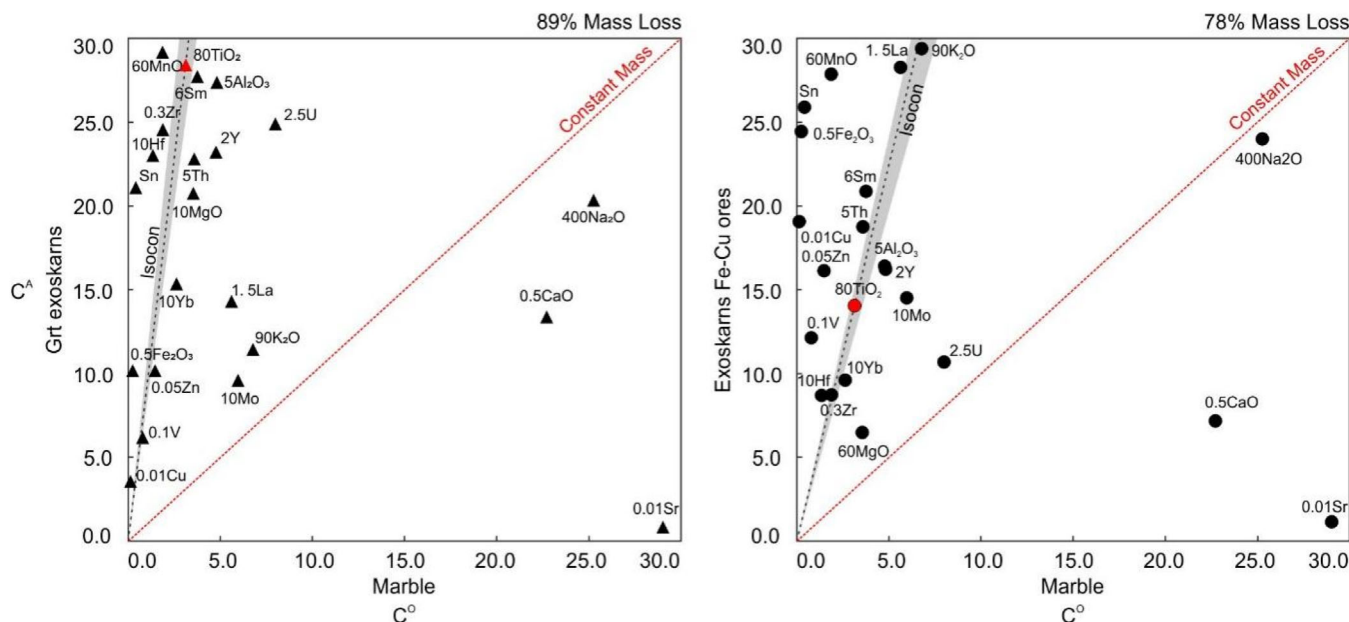


FIGURE 10 Isocon plots showing mass changes due to exoskarn formation in the Tonglushan system, specifically for: (a) Grt exoskarns; and (b) Fe–(Cu) exoskarns. Details related to the diagrams can be seen in Figure 8. Grt, garnet.

systems, as discussed above; and (2) alkali-rich (Anderson & Burnham, 1983). In the first case, at 250°C, total dissolved Al in fluids in equilibrium with alunite + kaolinite + quartz is ~2000 ppm at pH = 2 but drops to only ~1 ppm when the pH increases to 4 (Stoffregen, 1987).

In considering the potential role of alkali-rich solutions, an experimental study by Anderson and Burnham (1983) demonstrated that the transport of Al in hydrothermal fluids depends on free alkali ions being carried with Al as alkali-alumina complexes. The content of Al in a fluid in equilibrium with corundum ranges from 1.5×10^{-5} mol/kg H₂O (400°C, 1 kbar, and 10^{-3} M HCl solution) to 0.9 mol/kg H₂O (800°C, 5 kbar, and 1 M NaOH solution) (Azimov & Bushmin, 2007). For example, Nijland and Touret (2001), from studies in Mjåvatn, Norway, concluded that the replacement of pegmatite graphitic quartz + K-feldspar by graphitic albite + actinolite + clinopyroxene required large quantities of additional Al brought in by Al–NaCl-rich brines. Such brines could have therefore removed Al during the formation of the Tonglushan endoskarns and also caused sodic alteration where existing skarn minerals, e.g. granditic garnet and epidote, were crosscut by sodic plagioclase + chlorite + calcite veins (see fig. 13f in Zhang, Williamson, Rollinson, et al., 2023).

Sodic alteration (albite + chlorite + calcite) in the Tonglushan endoskarn and QMD also necessitated the addition of Na, probably derived from relatively cool Na-bearing fluids from, or which had interacted with, evaporite-bearing (including halite) portions of the

carbonate xenoliths and wall rocks of the Daye and Jialingjiang Formation (Zhu et al., 2017). Such sodic alteration has been reported in other porphyry-related systems worldwide, for example the Ann-Mason and Yerington deposit, Nevada (Carten, 1986; Dilles & Einaudi, 1992) and Ridgeway deposit, Australia (Wilson et al., 2003).

5.1.3 | Zr, Hf, U, and REEs

Zirconium, Hf, and U are relatively enriched in the prograde endoskarns (Figure 9a–c) and therefore the fluids from which they formed are likely to have contained elevated levels of these metals. This can be attributed to the fluids having a high activity of F (α_F), which is typical of alkalic, F-rich igneous systems (Gieré, 1990; Rubin et al., 1993; Smith et al., 2002), although it has also been suggested that Zr can be mobilized by sulphate complexes which form large polymerized units with bridging sulphate groups (Zr–SO₄–Zr) (Mottet et al., 1992; Rubin et al., 1993). However, the presence of igneous fluorapatite in the Tonglushan QMD with F contents of 3.2 wt % is consistent with a F-rich magmatic system (Nie et al., 2020). High F is also likely to have been a feature of the fluids responsible for the formation of the prograde endoskarns, as evident from the presence of hydrothermal fluorapatite with 2.8 ± 0.25 wt % F ($n = 51$) (Zhang, Williamson, & Broom-Fendley, 2023). As the F is likely to have been carried as HF (Shapovalov &

TABLE 3 Isocon analysis for K–Na-altered QMD and endoskarns in the Tonglushan system.

Element/ sample	QMD			Endoskarns (C_1^A)			Gain/loss relative to C_1^O					
	Least- altered (C_1^O) Avg. ($n = 2$)	K–Na- altered (C_1^A) Avg. ($n = 5$)	Grt veins/ salvages Di $n = 1$	Grt veins/ salvages Avg. ($n = 2$)	Grt- Di-Pl $n = 1$	Massive Grt		K–Na- altered	Di	Grt veins /salvages $\Delta C_1/C_1^O$ (100%)	Grt- Di-Pl	Massive Grt
						$n = 1$	Factor					
Al ₂ O ₃	15.4	14.5	16.7	17.2	12.8	10.2	1.0	1	-1	15	-9	-28
Fe ₂ O ₃	3.92	3.10	4.56	5.52	13.8	15.4	2.0	-18	6	46	283	326
MgO	1.34	1.10	2.39	2.93	0.89	0.64	10.0	-14	63	126	-28	-48
CaO	4.96	5.03	7.31	15.9	24.6	25.0	1.0	6	34	230	439	445
TiO ₂	0.55	0.53	0.60	0.53	0.50	0.50	25.0	0	0	0	0	0
P ₂ O ₅	0.26	0.25	0.29	0.24	0.18	0.23	50.0	2	4	-3	-21	-2
MnO	0.07	0.06	0.09	0.29	0.47	0.67	30.0	-11	22	359	673	998
Na ₂ O	4.46	4.38	5.24	2.13	0.74	0.07	5.0	2	7	-51	-82	-98
K ₂ O	3.09	3.37	0.72	1.95	0.87	1.40	5.0	14	-79	-35	-69	-51
S	0.24	0.25	0.11	0.10	0.21	0.12	20.0	9	-59	-58	-5	-46
Ba	1002	873	198	138	12.1	8.71	0.0	-9	-82	-86	-99	-99
Rb	70.6	60.5	5.12	48.4	43.0	96.4	0.3	-11	-93	-29	-34	48
Sr	1092	928	1346	1153	160	1133	0.0	-12	13	9	-84	-89
Y	16.0	15.3	16.6	15.0	15.4	18.1	1.0	0	-5	-3	5	23
Sb	0.06	0.10	0.09	0.80	0.20	0.56	30.0	57	32	1198	238	858
Cs	0.88	1.13	0.24	7.56	10.2	29.4	1.0	34	-75	789	1166	3528
Nb	18.3	18.0	17.9	23.8	24.8	7.37	1.0	2	-11	34	47	-56
Sn	1.20	1.25	1.43	3.06	6.63	10.0	2.0	8	9	163	502	806
Sc	6.66	6.34	7.01	6.16	5.73	6.97	4.0	-1	-4	-4	-6	13
V	74.8	66.7	81.0	42.6	83.6	73.8	0.3	-7	-1	-41	22	7
Zr	32.5	31.4	30.3	75.5	111	157	0.2	0	-15	140	272	422
Hf	1.23	1.26	1.19	2.30	2.84	3.83	6.0	7	-11	93	153	239
Pb	8.68	8.65	5.77	8.34	5.09	5.20	2.5	4	-39	-1	-36	-35
Th	9.12	9.33	7.51	10.7	10.7	9.03	1.8	7	-25	21	27	7
U	1.86	1.69	2.17	1.84	3.54	7.25	1.0	-5	7	2	108	323
Cu	11.2	52.2	5.62	15.5	15.1	11.6	0.1	385	-54	43	47	12
Zn	39.0	33.1	41.4	50.5	18.7	19.2	0.5	-12	-3	34	-48	-47
Mo	1.37	2.29	1.73	1.93	9.72	2.50	2.0	74	16	46	676	98

TABLE 3 (Continued)

Element/ sample	QMD			Endoskarns (C_1^A)			Gain/loss relative to C_1^O					
	Least- altered (C_1^O) Avg. ($n = 2$)	K–Na- altered (C_1^A) Avg. ($n = 5$)	Grt veins/ salvages Di $n = 1$	Grt veins/ salvages Avg. ($n = 2$)	Grt- Di-Pl $n = 1$	Massive Grt $n = 1$	Factor	K–Na- altered	Di	Grt veins /salvages $\Delta C_1/C_1^O$ (100%)	Grt- Di-Pl	Massive Grt
La	49.3	45.7	56.6	31.1	24.6	1108	0.2	-4	5	-35	-46	143
Ce	82.8	73.2	106	61.7	55.7	128	0.2	-8	17	-23	-27	68
Pr	10.4	9.72	12.2	7.53	6.58	10.2	2.0	-3	7	-25	-31	6
Nd	37.7	34.8	42.8	28.6	26.6	35.1	0.5	-4	4	-22	-23	1
Sm	6.63	6.09	7.22	5.81	5.42	6.87	4.0	-4	-1	-9	-11	12
Eu	1.74	1.57	1.77	1.27	1.38	1.87	5.0	-6	-7	-25	-14	16
Gd	4.77	4.47	5.28	4.44	4.31	5.41	5.0	-2	1	-4	-2	23
Tb	0.55	0.52	0.60	0.53	0.50	0.61	40.0	-2	-1	-1	0	20
Dy	3.17	3.03	3.48	3.01	3.06	3.74	8.0	0	0	-2	5	28
Ho	0.56	0.54	0.60	0.53	0.53	0.66	40.0	0	-2	-3	3	27
Er	1.60	1.51	1.69	1.48	1.55	1.86	15.0	-1	-3	-4	6	27
Tm	0.21	0.19	0.21	0.19	0.20	0.25	100	-2	-6	-7	4	30
Yb	1.38	1.32	1.44	1.35	1.38	1.65	5.0	0	-5	1	8	29
Lu	0.18	0.18	0.19	0.17	0.18	0.22	100	1	-5	0	11	33

Abbreviation: Di, diopside; Grt, garnet; Pl, plagioclase.

TABLE 4 Isocon analysis for K–Na-altered QMD and endoskarns in the Tonglushan system.

Element/sample	Marble (C_1^0) $n = 1$	Exoskarns (C_1^A)		Factor	Gain/loss relative to C_1^0	
		Massive Grt exoskarns $n = 1$	Fe–(Cu) exoskarn ores Avg. ($n = 7$)		Massive Grt exoskarns $\Delta C_i/C_1^0$ (100%)	Fe–Cu) exoskarn ores
Al ₂ O ₃	0.96	5.48	3.25	5.0	–37	–25
Fe ₂ O ₃	0.48	20.4	48.9	0.5	365	2157
MgO	0.35	2.08	0.65	10.0	–35	–59
CaO	45.4	26.8	14.4	0.5	–94	–93
TiO ₂	0.04	0.36	0.18	80.0	0	0
MnO	0.03	0.49	0.46	60.0	73	234
Na ₂ O	0.06	0.05	0.06	400	–91	–79
K ₂ O	0.08	0.13	0.33	90.0	–81	–4
Sr	2902	85.9	116	0.0	–100	–99
Y	3.17	15.5	11.0	1.5	–46	–23
Sn	0.40	21.1	25.9	1.0	481	1341
Sc	1.24	8.70	3.48	0.1	–23	–38
V	7.78	62.05	122	0.3	–12	247
Zr	6.23	81.90	29.1	10.0	44	4
Hf	0.13	2.30	0.87	5.0	89	45
Cu	14.9	449	2387	2.5	232	3465
Zn	29.2	204	323	0.0	–23	146
Mo	0.59	0.96	1.45	0.1	–82	–46
La	3.74	9.55	18.9	10.0	–72	12
Sm	0.62	4.63	3.48	1.5	–19	24
Eu	0.13	1.59	1.38	6.0	36	139
Yb	0.26	1.54	0.96	10.0	–36	–18

Abbreviation: Grt, garnet.

Setkova, 2012), the F-rich fluids will have caused the dissolution of silicate minerals (Chang & Meinert, 2004, 2008), including zircon which is present in the precursor QMD. This scheme is consistent with those suggested for the formation of endoskarns worldwide (Empire deposit; Chang & Meinert, 2004, 2008; Taocun deposit; Zeng et al., 2016).

The formation of garnet-bearing skarns—that is, garnet endoskarns (including massive garnet and garnet veins/salvages) and garnet-diopside-plagioclase endoskarn—appears to have been associated with considerable addition of Zr, Hf, and U (Figure 9a–c; Table 3). These elements can be incorporated in Zr- and U-rich minerals such as zircon and zirconolite (Gieré, 1986), or skarn minerals such as garnet (Katerinopoulou et al., 2009; Lupini et al., 1992). In the Tonglushan system, no zircon and zirconolite have been identified in the endoskarn, although allanite, which typically contains small amounts of U (Gieré & Sorensen, 2004), is present

in the garnet endoskarn (Zhang, Williamson, Rollinson, et al., 2023). Previous studies show that large concentrations of Zr can be incorporated in garnet through substitution for Ti (Deer et al., 2013), and/or Al³⁺ or Fe³⁺ in the octahedral site with a corresponding tetrahedral substitution of Al³⁺ for Si⁴⁺ to maintain charge balance (Munno et al., 1980). It is therefore likely that Zr and Hf are mainly hosted in the garnet of the garnet-bearing endoskarns at Tonglushan (Degeling et al., 2001; Mezger et al., 1989), as evidenced from the presence of up to 30 ppm of Hf in the garnet of the endoskarns (Zhang et al., 2019). Uranium could also have been incorporated into garnet in the Tonglushan endoskarn, probably due to the replacement of Ca²⁺ with U⁴⁺ in the dodecahedral sites of the garnet crystal structure (Mezger et al., 1989).

The Tonglushan endoskarns are particularly enriched in REE, with an apparent addition of up to 143% La and 68% Ce which are mostly, in all likelihood, hosted in allanite (REE,Ca)₂(Al,Fe)₃(SiO₄)₃(OH). That the allanite

crystallized during the retrograde skarn stage is evident from its absence in the QMD and prograde skarn assemblages. The most likely explanation for the relatively high REE in the endoskarn is their introduction via F-bearing fluids (Gieré, 1986; Smith et al., 2002). REE can be mobile in solutions rich in F^- , Cl^- , HCO_3^- , CO_3^{2-} , HPO_4^{2-} , PO_4^{3-} , or with a combination of such ligands (Cui et al., 2020; Lottermoser, 1992; Migdisov et al., 2019; Wan et al., 2021; Williams-Jones & Migdisov, 2014). Skarn-forming fluids typically contain chloride-complexes (e.g., Meinert et al., 2005) but fluoride ligands (also enhancing Zr, Hf and U solubility as mentioned above) are considered to be the main control on hydrothermal mobilization of REE (Gieré, 1986, 1990; Pan & Fleet, 1990; Smith et al., 2002). For example, Smith et al. (2002) suggested that allanite in endoskarns in the Beinn an Dubhaich granite, Isle of Skye, crystallized from F-rich aqueous fluids. The abundance of phlogopite ($KMg_3AlSi_3O_{10}(F,OH)_2$) in the Tonglushan retrograde exoskarn assemblages (Zhao et al., 2012) also suggests that the fluids were F-bearing and therefore very capable of transporting REE.

5.2 | Mass changes due to endoskarn formation

The formation of endoskarn within magmatic bodies emplaced into carbonates (now marble locally) has been generally interpreted to result from Ca-metasomatism, which involves migration of large amounts of Ca from surrounding carbonates (e.g., Einaudi, 1982). The Tonglushan QMD underwent an addition of up to 445% Ca to form the prograde endoskarns (Figure 9; Table 3), producing mainly garnet, diopside and plagioclase (Figure 4c–f), and the carbonate underwent an 89% mass loss and 94% removal of Ca (Figure 10; Table 4), although some Ca may have been sourced from the breakdown of plagioclase and hornblende phenocrysts during muscovite alteration in the QMD, or from the magmatic-hydrothermal fluids.

The mechanism of migration of Ca from the carbonates into the adjacent QMD is still unclear. In such settings, it is usually interpreted to be due to solid-state or intra-fluid diffusion (Dyer et al., 2011; Fulignati et al., 2000) or by flow of Ca–CO₂–bearing fluids released as a result of decarbonation of carbonates during exoskarn formation (Shen et al., 2013). Both processes may be accompanied by reverse transport of components (e.g., Fe, Mn, Sn, and Si) from the QMD magmas into the carbonates, as evidenced by a 365% increase in Fe₂O₃, 73% in MnO and 481% in Sn in the formation of the garnet exoskarns (Table 4). The contacts between the magma and surrounding carbonates were probably

saturated with fluids derived from the magmas and pore waters from the carbonates (e.g., Meinert et al., 2005). If the chemical potential gradients for Ca were high, and in an appropriate direction, diffusion via fluids could go against the direction of overall advective circulation (Woodford et al., 2001). In addition, the reactions may have proceeded more easily and completely where fluids were abundant along the contact with surrounding carbonates. Evidence for the migration of Ca via hydrothermal fluids is the formation of garnet and diopside veins (Figure 4e, f) further inside the pluton; such a process could have been controlled directly by fractures in the outer part of the QMD. Despite the possible role of fluids in fractures, diffusion is likely to have been a more important mechanism in endoskarn formation as the massive garnet endoskarn underwent much more Ca addition than garnet veins/salvages (445% vs. 230% gain of Ca; Table 3), and endoskarnification is usually pervasive rather than proximal to veins.

Fe₂O₃, MnO, and Sn, which, due to their low concentrations in the carbonate wall rocks, were mainly derived from magmatic-hydrothermal fluids, were added during endoskarn formation (Table 3). The prograde skarn stage mostly involved the replacement of variously altered QMD with granditic garnet which is generally Fe³⁺-rich (Adr_{40.5}Grs_{56.9} to Adr_{78.0}Grs_{20.2}) and contains high concentrations of MnO (0.46–0.79 wt %) (Zhang, Williamson, Rollinson, et al., 2023). Tin is likely to have been incorporated into the Fe-rich garnet as the massive garnet endoskarn has much higher Sn than the diopside endoskarn (10.0 versus 1.4 ppm; Table 3). This incorporation was probably due to the substitution $3Sn^{4+} + [] = 4Fe^{3+}$ ($[]$ = a divalent cations-site vacancy in the octahedral site; Yu et al., 2020) in the garnet under relatively oxidizing conditions (Ding et al., 2018; Park et al., 2017) during the formation of the prograde endoskarns. Subsequent retrograde endoskarnification (allanite ± epidote ± chlorite ± calcite) and potassic (biotite + hematite ± quartz) alteration, again occurred under relatively oxidizing conditions, as suggested from the incorporation of significant Fe³⁺ in these mineral assemblages. The fluids were therefore relatively oxidizing throughout the paragenesis of endoskarn formation.

Alkali elements (Na, K, Ba, Sr, and Rb) were extensively removed during the formation of the prograde endoskarns (Figure 9), due to replacement of existing minerals (mainly feldspars and muscovite) with calc-silicates such as garnet. The release of Na likely contributed to the crystallization of plagioclase in the prograde skarn assemblage. However, there was no obvious sink for K in prograde and retrograde skarn minerals (e.g., garnet, diopside, allanite, and epidote). Potassium and Na would thus have been incorporated into potassic (e.g., K-feldspar) and sodic (e.g., albite) assemblages in

the QMD distal to the endoskarn, or transported into the exoskarn to form such minerals as phlogopite and scapolite (Zhao et al., 2012), or underwent fluid escape via structures (Meinert et al., 2005).

Copper was strongly enriched in the exoskarns compared with the potassic-sodic-altered QMD (~3500% vs. 385% addition of Cu; Tables 3 and 4). Such significant addition is due to the precipitation of Cu–Fe sulphides in sulphide-(quartz) veins and as replacements after earlier Fe-rich alteration minerals in the exoskarns (Zhao et al., 2012). The potassic-sodic-altered QMD shows a strong addition of Cu, at least compared with the endoskarns (~385% vs. 12% increase; Table 3), which is consistent with the precipitation of Cu–Fe sulphides within the potassic alteration assemblage (porphyry-style mineralization).

5.3 | Endoskarn-exoskarn- versus porphyry-style alteration and mineralization

In porphyry systems with an endoskarn-exoskarn pairing, Cu ores are generally restricted to the exoskarns (Einaudi & Burt, 1982), although there are some exceptions where primary Cu mineralization occurs in both the exoskarns and endoskarns (e.g., Antamina, Peru: Redwood, 2004; Empire, Idaho: Chang & Meinert, 2004).

The poorly mineralized nature of the Tonglushan endoskarns is probably because they formed under relatively oxidizing conditions, as evidenced from the significant addition of Fe³⁺ (Figure 9), mostly incorporated in granditic garnet, epidote, allanite and hematite. During endoskarn formation, the relatively oxidizing conditions likely restricted the precipitation of sulphides and rather allowed fluids to carry Cu into surrounding exoskarns.

Pervasive dissolution of surrounding carbonates in the process of exoskarnification will have neutralized and cooled the ore-forming fluids and provided open space for sulphide precipitation. During the formation of prograde garnet exoskarn, for example, carbonate xenoliths underwent significant mass loss of up to 89% (Figure 10). Calcium was transported, probably mostly by diffusion, in the reverse direction into the QMD to form calc-silicates in the endoskarns. Importantly, rather than moving into the endoskarns to precipitate carbonate, much of the CO₂ produced during exoskarnification moved upwards and out of the exoskarn through fractures, which could have caused the formation of the breccias seen in overlying carbonate country rocks (see geological map in Figure 2). The simultaneous movement of ore-forming fluids into the exoskarns was favored due to dissolution of carbonate and the creation of open space and therefore relatively low-

pressure zones. In addition, a chimney effect, drawing fluids from the QMD into the wall rocks, was produced by the upwards migration of CO₂-rich fluids from the carbonates undergoing exoskarnification, in a positive feedback loop to increase alteration and mineralization in the exoskarns. As a result, metals (e.g., Cu) were more likely transported into carbonate wall rocks by magmatic-hydrothermal fluids, rather than migrating upwards through the QMD stock to form porphyry-style mineralization. That this mechanism was important in the Tonglushan system is evidenced by the presence of large-scale endoskarns which mark a zone of lateral through flow of magmatic-hydrothermal fluids towards the extensively mineralized exoskarns. This may go some way to explain the rare co-occurrence of large volume endoskarns together with major porphyry-style deposits, with or without exoskarns, in porphyry systems.

This finding offers a new criterion for exploration for porphyry-related deposits in carbonate-rich terranes worldwide. It is suggested that in a prospective magmatic terrane, for example in the MLYRB, one of the first steps should be to investigate the presence and volumes of endoskarn and exoskarn. The likelihood of the system hosting an economic porphyry-style deposit will decrease if there is extensive endoskarn. Discriminating endo- from exo-skarns, however, can be problematic as it relies on the identification of textures inherited from the protolith, for example, magmatic relics indicating endoskarn, which are not always apparent. If not possible, then endoskarns and exoskarns could potentially be discriminated from their whole-rock geochemical characteristics (e.g., chemical changes identified from isocon analysis), as they formed from different protoliths and underwent distinct chemical exchanges. It is also important to look for hydrothermal breccias in overlying and surrounding units, which may be indicative of carbonate dissolution and the chimney affect which could have drawn potentially mineralising hydrothermal fluids from the parent intrusive, through the endoskarn, causing further and more widespread endoskarnification, and into the exoskarn; such a process would reduce the likelihood of porphyry-style mineralization in and around the magmatic stock and increase the potential for exoskarn deposits. We believe that these aspects should be incorporated into future exploration models for porphyry-skarn-type deposits.

6 | CONCLUSIONS

Mass change calculations have been used to explain geochemical trends during potassic-sodic alteration (porphyry-style alteration and mineralization), endoskarn

formation in the QMD, and exoskarnification of the carbonate xenoliths and wall rocks of the Tonglushan system. The mobility of some HFSE (i.e., Zr, Hf, U, and REE) during endoskarn formation was likely facilitated by high αF , whereas Al was mobile later in endoskarn formation, possibly due to the involvement of Na-rich fluids which also caused sodic alteration. Endoskarn formation involved the reverse migration of Ca into the QMD pluton from the exoskarnification of carbonate xenoliths and wall rocks, possibly via both diffusion and migration of metasomatic fluids. Iron and Mn were mainly sourced from magmatic-hydrothermal fluids that were added in the garnet-bearing endoskarns, whereas alkali elements (e.g., Na, K, and Rb) were removed due to the replacement of plagioclase, hornblende and K-feldspar phenocrysts with prograde skarn minerals. These alkali elements may have contributed to the formation of sodic alteration assemblages in the QMD distal to the endoskarn and/or to the peripheral exoskarns. Conditions were relatively oxidizing within the endoskarn environment, so limiting sulphide precipitation. The magmatic-hydrothermal fluids were drawn into the xenoliths and wall rocks due to there being relatively low-pressure zones (open space) in the carbonates formed because of carbonate dissolution. The upwards loss of CO_2 caused a chimney effect which drew more metal-bearing fluids into the carbonates. The magmatic-hydrothermal fluids, when entering the carbonates, underwent a dramatic change in pH, and a decrease in pressure and temperature, which aided the precipitation of sulphides. In addition, the higher porosity and permeability of the endoskarns compared with the surrounding QMD may have promoted the lateral flow of Cu-bearing fluids to mineralize the exoskarns, rather than upwards flow within the QMD stock to produce porphyry-style alteration and mineralization. These findings offer new constraints for exploration models for porphyry-skarn-related mineral deposits.

ACKNOWLEDGMENTS

This research was financed by a China Scholarship Council and University of Exeter PhD Scholarship to the first author. The authors would like to thank Prof Jun Tan from China University of Geosciences (Wuhan), and geologists from the Geological Bureau First Geological Brigade for providing assistance during fieldwork. We thank Miss Sharon Uren for ICP-MS analyses at the CSM, University of Exeter. Arifudin Idrus, Saeed Alirezaei and two anonymous reviewers are gratefully acknowledged for comments on the manuscript.

CONFLICT OF INTEREST STATEMENT


Authors declare no conflict of interests for this article.

DATA AVAILABILITY STATEMENT

Data available on request from the authors.

ORCID

Fei Zhang  <https://orcid.org/0000-0002-0468-6594>

Ben J. Williamson  <https://orcid.org/0000-0002-2639-3725>

REFERENCES

- Ahmed, A.D., Hood, S.B., Gazley, M.F., Cooke, D.R. & Orovan, E.A. (2019) Interpreting element addition and depletion at the Ann Mason porphyry-Cu deposit, Nevada, using mapped mass balance patterns. *Journal of Geochemical Exploration*, 196, 81–94.
- Anderson, G.M. & Burnham, C.W. (1983) Feldspar solubility and the transport of aluminum under metamorphic conditions. *American Journal of Science*, 283, 283–297.
- Angiboust, A. & Harlov, D. (2017) Ilmenite breakdown and rutile-titanite stability in metagranitoids: natural observations and experimental results. *American Mineralogist*, 102, 1696–1708.
- Azimov, P.Y. & Bushmin, S.A. (2007) Solubility of minerals of metamorphic and metasomatic rocks in hydrothermal solutions of varying acidity: thermodynamic modeling at 400–800°C and 1–5 kbar. *Geochemistry International*, 45, 1210–1234.
- Cail, T.L. & Cline, J.S. (2001) Alteration association with gold deposition at the Getchell Carlin-type gold deposit, north-Central Nevada. *Economic Geology*, 96, 1343–1359.
- Carten, R.B. (1986) Sodium-calcium metasomatism: chemical, temporal, and spatial relationships at the Yerington, Nevada porphyry copper deposit. *Economic Geology*, 81, 1495–1519.
- Chang, Z.S. & Meinert, L.D. (2004) The magmatic-hydrothermal transition: evidence from quartz phenocryst textures and endoskarn abundance in Cu-Zn skarns at the empire mine, Idaho USA. *Chemical Geology*, 210, 149–171.
- Chang, Z.S. & Meinert, L.D. (2008) The empire Cu-Zn mine, Idaho: exploration implications of unusual skarn features related to high fluorine activity. *Economic Geology*, 103, 909–938.
- Chu, G., Chen, H., Falloon, T.J., Han, J., Zhang, S., Cheng, J. et al. (2020) Early cretaceous mantle upwelling and melting of juvenile lower crust in the middle-lower Yangtze River Metallogenic Belt: example from Tongshankou Cu-(Mo-W) ore deposit. *Gondwana Research*, 83, 183–200.
- Cui, H., Zhong, R.C., Xie, Y.L., Yuan, X.Y., Liu, W.H., Brugger, J. et al. (2020) Forming sulfate- and REE-rich fluids in the presence of quartz. *Geology*, 48, 145–148.
- Dana, C.D.P., Agangi, A., Takahashi, R., Idrus, A. & Lai, C.K. (2022) Element mobility during formation of the Ruwai Zn-Pb-Ag skarn deposit, Central Borneo, Indonesia. *Resource Geology*, 72, e12290.
- Deer, W.A., Howie, R.A. & Zussman, J. (2013) *An introduction to the rock-forming minerals*. Great Britain, Ireland: Mineralogical Society, pp. 230–233.
- Degeling, H., Eggins, S. & Ellis, D.J. (2001) Zr budgets for metamorphic reactions, and the formation of zircon from garnet breakdown. *Mineralogical Magazine*, 65, 749–758.
- Dilles, J.H. & Einaudi, M.T. (1992) Wall-rock alteration and hydrothermal flow paths about the Ann-Mason porphyry copper deposit, Nevada: a 6-km vertical reconstruction. *Economic Geology*, 87, 1963–2001.

- Ding, T., Ma, D.S., Lu, J.J. & Zhang, R.Q. (2018) Garnet and scheelite as indicators of multi-stage tungsten mineralization in the Huangshaping deposit, southern Hunan province, China. *Ore Geology Reviews*, 94, 193–211.
- Duan, D.F. & Jiang, S.Y. (2017) In situ major and trace element analysis of amphiboles in quartz monzodiorite porphyry from the Tonglvshan Cu–Fe (Au) deposit, Hubei Province, China: insights into magma evolution and related mineralization. *Contributions to Mineralogy and Petrology*, 172, 1–17.
- Dyer, B., Lee, C.T.A., Leeman, W.P. & Tice, M. (2011) Open-system behavior during pluton-wall-rock interaction as constrained from a study of endoskarns in the Sierra Nevada batholith, California. *Journal of Petrology*, 52, 1987–2008.
- Einaudi, M.T. (1982) Description of skarns associated with porphyry copper plutons, southwestern North America. In: Titley, S.R. (Ed.) *Advances in geology of the porphyry copper deposits: southwestern North America*. Tucson: University of Arizona Press, pp. 239–248.
- Einaudi, M.T. & Burt, D.M. (1982) Introduction-terminology, classification, and composition of skarn deposits. *Economic Geology*, 77, 745–754.
- Finlow-Bates, T. & Stumpfl, E.F. (1981) The behaviour of so-called immobile elements in hydrothermally altered rocks associated with volcanogenic submarine-exhalative ore deposits. *Mineralium Deposita*, 16, 319–328.
- Fulignati, P., Marianelli, P., Santacroce, R. & Sbrana, A. (2000) The skarn shell of the 1944 Vesuvius magma chamber. Genesis and P-T-X conditions from melt and fluid inclusion data. *European Journal of Mineralogy*, 12, 1025–1039.
- Gieré, R. (1986) Zirconolite, allanite and hoegbomite in a marble skarn from the Bergell contact aureole: implications for mobility of Ti, Zr and REE. *Contributions to Mineralogy and Petrology*, 93, 459–470.
- Gieré, R. (1990) Hydrothermal mobility of Ti, Zr and REE: examples from the Bergell and Adamello contact aureoles (Italy). *Terra Nova*, 2, 60–67.
- Gieré, R. & Sorensen, S.S. (2004) Allanite and other: REE-rich epidote-group minerals. *Reviews in Mineralogy and Geochemistry*, 56, 431–493.
- Grant, J.A. (1986) The isocon diagram: a simple solution to Gresens' equation for metasomatic alteration. *Economic Geology*, 81, 1976–1982.
- Grant, J.A. (2005) Isocon analysis: a brief review of the method and applications. *Physics and Chemistry of the Earth*, 30, 997–1004.
- Gresens, R.L. (1967) Composition-volume relationships of metasomatism. *Chemical Geology*, 2, 47–65.
- Karimzadeh Somarin, A. (2004) Geochemical effects of endoskarn formation in the Mazraeh Cu-Fe skarn deposit in northwestern Iran. *Geochemistry: Exploration, Environment, Analysis*, 4, 307–315.
- Karimzadeh Somarin, A. (2010) Garnetization as a ground prepa-process for copper mineralization: evidence from the Mazraeh skarn deposit, Iran. *International Journal of Earth Sciences*, 99, 343–356.
- Katerinopoulou, A., Katerinopoulos, A., Voudouris, P., Bieniok, A., Musso, M. & Amthauer, G. (2009) A multi-analytical study of the crystal structure of unusual Ti-Zr-Cr-rich andradite from the Maronia skarn, Rhodope massif, western Thrace, Greece. *Mineralogy and Petrology*, 95, 113–124.
- Kouzmanov, K. & Pokrovski, G.S. (2012) Hydrothermal controls on metal distribution in porphyry Cu (-Mo-Au) systems. *Geology*, 16, 573–618.
- Large, R.R., Gemmel, J.B. & Paulick, H. (2001) The alternation box plot: a simple approach to understanding the relationship between alteration mineralogy and litho-geochemistry associated with volcanic-hosted massive sulfide deposits. *Economic Geology*, 96, 957–971.
- Lentz, D.R. (2005) Mass-balance analysis of mineralized skarn systems: implications for replacement processes, carbonate mobility, and permeability evolution. In: *Mineral deposit research: meeting the global challenge*. Berlin Heidelberg: Springer, pp. 421–424.
- Li, J.W., Deng, X.D., Zhou, M.F., Liu, Y.S., Zhao, X.F. & Guo, J.L. (2010) Laser ablation ICP-MS titanite U-Th-Pb dating of hydrothermal ore deposits: a case study of the Tonglushan Cu-Fe-Au skarn deposit, SE Hubei Province, China. *Chemical Geology*, 270, 56–67.
- Li, J.W., Zhao, X.F., Zhou, M.F., Ma, C.Q., Souza, Z.S. & Vasconcelos, P. (2009) Late Mesozoic magmatism from the Daye region, eastern China: U-Pb ages, petrogenesis, and geodynamic implications. *Contributions to Mineralogy and Petrology*, 157, 383–409.
- Li, J.-W., Vasconcelos, P. M., Zhou, M.-F., Deng, X.-D., Cohen, B., Bi, S.-J. et al. (2014) Longevity of magmatic-hydrothermal systems in the Daye Cu-Fe-Au District, eastern China with implications for mineral exploration. *Ore Geology Reviews*, 57, 375–392.
- Liu, X.N., Kong, F.H., Yang, P., Liu, Z.M., Zhu, L. & Li, H. (2009) Distribution and basic characteristics of small intrusions in southern Hubei. *Resource Environmental Engineering*, 23, 390–395 (in Chinese with English abs.).
- Lottermoser, B.G. (1992) Rare earth elements and hydrothermal ore formation processes. *Ore Geology Reviews*, 7, 25–41.
- Lupini, L., Williams, C.T. & Woolley, A.R. (1992) Zr-rich garnet and Zr- and Th-rich perovskite from the Polino carbonatite, Italy. *Mineralogical Magazine*, 56, 581–586.
- Mathieu, L. (2018) Quantifying hydrothermal alteration: a review of methods. *Geosciences*, 8, 245.
- Meinert, L.D., Dipple, G.M. & Nicolescu, S. (2005) World skarn deposits. *Economic Geology*, 100, 299–336.
- Meyer, C. & Hemley, J.J. (1967) Wall rock alteration. In: Barnes, H.-L. (Ed.) *Geochemistry of hydrothermal ore deposits*. New York: Holt, Rinehart, and Winston, pp. 166–235.
- Mezger, K., Hanson, G.N. & Bohlen, S.R. (1989) U-Pb systematics of garnet: dating the growth of garnet in the late Archean Pikwitonei granulite domain at Cauchon and Natawahunan Lakes, Manitoba, Canada. *Contributions to Mineralogy and Petrology*, 101, 136–148.
- Migdisov, A.A., Xu, H.W., Williams-Jones, A.E. & Brugger, J. (2019) The REEs in hydrothermal systems. In: Maurice, P. (Ed.) *Encyclopedia of water. Science, technology, and society*. Hoboken: John Wiley & Sons.
- Montreuil, J.F., Potter, E.G., Corriveau, L. & Davis, W.J. (2016) Element mobility patterns in magnetite-group IOCG systems: the fab IOCG system, Northwest Territories, Canada. *Ore Geology Reviews*, 72, 562–584.
- Mottet, B., Pichavant, M., Bény, J. & Alary, J. (1992) Morphology of zirconia synthesized hydrothermally from zirconium oxychloride. *Journal of the American Ceramic Society*, 75, 2515–2519.

- Mrozek, S.A., Chang, Z., Spandler, C., Windle, S., Raraz, C. & Paz, A. (2020) Classifying skarns and quantifying metasomatism at the Antamina deposit, Peru: insights from whole-rock geochemistry. *Economic Geology*, 115, 177–188.
- Munno, R., Rossi, G. & Tadini, C. (1980) Crystal chemistry of kimeyite from Stromboli, Aeolian Islands, Italy. *American Mineralogist*, 65, 188–191.
- Nie, L.Q., Zhou, T.F., White, N., Wang, F.Y. & Song, Y.L. (2020) Zircon geochemistry of Edong granitoids in the middle-lower Yangtze Metallogenic Belt (eastern China): constraints on W-Cu-Fe skarn mineralization. *Ore Geology Reviews*, 120, 103461.
- Nijland, G. & Touret, L.R. (2001) Replacement of graphic pegmatite by graphic albite-actinoliteclinopyroxene intergrowths (Mjavatn, southern Norway). *European Journal of Mineralogy*, 13, 41–50.
- Pan, Y.M. & Dong, P. (1999) The lower Changjiang (Yangzi/Yangtze River) metallogenic belt, east Central China: intrusion- and wall rock-hosted Cu-Fe-Au, Mo, Zn, Pb, Ag deposits. *Ore Geology Reviews*, 15, 177–242.
- Pan, Y.M. & Fleet, M.E. (1990) Halogen-bearing allanite from the white river gold occurrence, hemlo area, Ontario. *The Canadian Mineralogist*, 28, 67–75.
- Park, C., Choi, W., Kim, H., Park, M.-H., Kang, I.M., Lee, H.-S. et al. (2017) Oscillatory zoning in skarn garnet: implications for tungsten ore exploration. *Ore Geology Reviews*, 89, 1006–1018.
- Pilote, J.L., Piercey, S.J. & Mercier-Langevin, P. (2020) Evolution of the seafloor hydrothermal system associated with the Ming VMS deposit, Newfoundland Appalachians, and its controls on base and precious metal distribution. *Mineralium Deposita*, 55, 913–936.
- Redwood, S.D. (2004) Geology and development history of the Antamina copper-zinc skarn deposit, Peru. *Society of Economic Geologists*, 11, 259–277.
- Rubin, J.N., Henry, C.D. & Price, J.G. (1993) The mobility of zirconium and other “immobile” elements during hydrothermal alteration. *Chemical Geology*, 110, 29–47.
- Shapovalov, Y.B. & Setkova, T.V. (2012) Experimental study of mineral equilibria in the system $K_2O(Li_2O)-Al_2O_3-SiO_2-H_2O-HF$ at 300 to 600°C and 100 MPa with application to natural greisen systems. *American Mineralogist*, 97, 1452–1459.
- Shen, B., Wimpenny, J., Lee, C.T.A., Tollstrup, D. & Yin, Q.Z. (2013) Magnesium isotope systematics of endoskarns: implications for wallrock reaction in magma chambers. *Chemical Geology*, 356, 209–214.
- Shu, Q.A., Chen, P.R. & Chen, J.R. (1992) *Geology of Fe-Cu ore deposits in eastern Hubei Province*. Beijing: Press of Metallurgical Industry. 510 (in Chinese).
- Sillitoe, R. H. (2010). Porphyry copper systems. *Economic Geology*, 105(1), 3–41.
- Smith, M.P., Henderson, P. & Jeffries, T. (2002) The formation and alteration of allanite in skarn from the Beinn an Dubhaich granite aureole, Skye. *European Journal of Mineralogy*, 14, 471–486.
- Stoffregen, R. (1987) Genesis of acid-sulfate alteration and Au-Cu-Ag mineralization at Summitville, Colorado. *Economic Geology*, 82, 1575–1591.
- Tomlinson, D.H., Christiansen, E.H., Keith, J.D., Dorais, M.J., Ganske, R., Fernandez, D. et al. (2021) Nature and origin of zoned polymetallic (Pb-Zn-Cu-Ag-Au) veins from the bingham canyon porphyry Cu-Au-Mo deposit, Utah. *Economic Geology*, 116, 747–771.
- Tropper, P. & Manning, C.E. (2005) Very low solubility of rutile in H_2O at high pressure and temperature, and its implications for Ti mobility in subduction zones. *American Mineralogist*, 90, 502–505.
- Van Baalen, M.R. (1993) Titanium mobility in metamorphic systems: a review. *Chemical Geology*, 110, 233–249.
- Wan, Y., Wang, X.L., Chou, I.M. & Li, X.C. (2021) Role of sulfate in the transport and enrichment of REE in hydrothermal systems. *Earth and Planetary Science Letters*, 569, 117068.
- Warr, L.N. (2021) IMA–CNMNC approved mineral symbols. *Mineralogical Magazine*, 85, 291–320.
- Wilkinson, J.J., Crowther, H.L. & Coles, B.J. (2011) Chemical mass transfer during hydrothermal alteration of carbonates: controls of seafloor subsidence, sedimentation and Zn-Pb mineralization in the Irish carboniferous. *Chemical Geology*, 289, 55–75.
- Williams-Jones, A.E. & Migdisov, A.A. (2014) Experimental constraints on the transport and deposition of metals in ore-forming hydrothermal systems. *Society of Economic Geologists*, 18, 77–98.
- Williams-Jones, A.E., Samson, I.M., Ault, K.M., Gagnon, J.E. & Fryer, B.J. (2010) The genesis of distal zinc skarns: evidence from the Mochito deposit, Honduras. *Economic Geology*, 105, 1411–1440.
- Wilson, A.J., Cooke, D.R. & Harper, B.L. (2003) The ridgeway gold-copper deposit: a high-grade alkalic porphyry deposit in the Lachlan fold belt, New South Wales, Australia. *Economic Geology*, 98, 1637–1666.
- Woodford, D.T., Sisson, V.B. & Leeman, W.P. (2001) Boron metasomatism of the Alta stock contact aureole, Utah: evidence from borates, mineral chemistry, and geochemistry. *American Mineralogist*, 86, 513–533.
- Xie, G.Q., Mao, J.W. & Zhao, H.J. (2011) Zircon U-Pb geochronological and Hf isotopic constraints on petrogenesis of late Mesozoic intrusions in the Southeast Hubei Province, middle-lower Yangtze River belt (MLYRB), East China. *Lithos*, 125, 693–710.
- Xie, G.Q., Mao, J.W., Zhao, H.J., Wei, K.T., Jin, S.G., Pan, H.J. et al. (2011) Timing of skarn deposit formation of the Tonglushan ore district, southeastern Hubei Province, middle-lower Yangtze River valley metallogenic belt and its implications. *Ore Geology Reviews*, 43, 62–77.
- Xie, G.Q., Zhu, Q.Q., Yao, L., Wang, J. & Li, W. (2013) Discussion on regional metal mineral deposit model of late Mesozoic Cu-Fe-Au polymetallic deposits in the Southeast Hubei province. *Bulletin of Mineralogy, Petrology and Geochemistry*, 32, 418–426 (in Chinese with English abs.).
- Xiong, X.L., Adam, J. & Green, T.H. (2005) Rutile stability and rutile/melt HFSE partitioning during partial melting of hydrous basalt: implications for TTG genesis. *Chemical Geology*, 218, 339–359.
- Yu, F., Shu, Q.H., Niu, X.D., Xing, K., Li, L.L., Lentz, D.R. et al. (2020) Composition of garnet from the Xianghualing skarn Sn deposit, South China: its significance and exploration potential. *Minerals*, 10, 456.
- Zeng, L.P., Zhao, X.F., Li, X.C., Hu, H. & McFarlane, C. (2016) In situ elemental and isotopic analysis of fluorapatite from the

- Taocun magnetite-apatite deposit, eastern China: constraints on fluid metasomatism. *American Mineralogist*, 101, 2468–2483.
- Zhai, Y.S., Xiong, Y.L., Yao, S.Z. & Lin, X.D. (1996) Metallogeny of copper and iron deposits in the eastern Yangtse craton, east-Central China. *Ore Geology Reviews*, 11, 229–248.
- Zhang, F., Williamson, B.J., Rollinson, G.K. & Hughes, H.S.R. (2023) A mineralogical investigation into the formation of ore-barren endoskarn: an example from the Tonglushan porphyry system, eastern China. *Ore Geology Reviews*, 157, 105441.
- Zhang, F., Williamson, B.J. & Broom-Fendley, S. (2023) Apatite texture and composition in the Tonglushan porphyry-related skarn system, eastern China: Implications for mineral exploration. *Ore Geology Reviews*, 158, 105441.
- Zhang, S.T., Chen, H.Y., Han, J.S., Zhang, Y., Chu, G.B., Wei, K.T. et al. (2018) Geochronology, geochemistry, and mineralization of quartz monzodiorite and quartz monzodiorite porphyry in Tonglushan Cu-Fe-Au deposit, Edongnan ore district, China. *Geochimica*, 47, 240–256 (in Chinese with English abs.).
- Zhang, S.T., Chen, H.Y., Shu, Q.H., Zhang, Y., Chu, G.B., Cheng, J.M. et al. (2019) Unveiling growth histories of multi-generational garnet in a single skarn deposit via newly-developed LA-ICP-MS U Pb dating of grandite. *Gondwana Research*, 73, 65–76.
- Zhang, S.T., Chu, G.B., Cheng, J.M., Zhang, Y., Tian, J., Li, J. et al. (2020) Short wavelength infrared (SWIR) spectroscopy of phyllosilicate minerals from the Tonglushan Cu-Au-Fe deposit, eastern China: new exploration indicators for concealed skarn orebodies. *Ore Geology Reviews*, 122, 103516.
- Zhang, S.T., Ma, Q., Chen, H.Y., Long, X.P., Chu, G.B., Zhang, W.F. et al. (2021) Petrogenesis of early cretaceous granitoids and mafic microgranular enclaves from the giant Tonglushan Cu-Au-Fe skarn orefield, Eastern China. *Lithos*, 392–393, 106103.
- Zhang, Y., Tian, J., Hollings, P., Gong, L., Albuero, I., Berador, A.E. et al. (2020) Mesozoic porphyry Cu-Au mineralization and associated adakite-like magmatism in The Philippines: insights from the giant atlas deposit. *Mineralium Deposita*, 55, 881–900.
- Zhao, H.J., Xie, G.Q., Wei, K.T. & Ke, Y.F. (2012) Mineral compositions and fluid evolution of the Tonglushan skarn Cu-Fe deposit, SE Hubei, east-Central China. *International Geology Review*, 54, 737–764.
- Zhao, S.G., Brzozowski, M.J., Mueller, T., Wang, L.J. & Li, W.Q. (2022) Skarn classification and element mobility in the Yeshan iron deposit, eastern China: insight from litho-geochemistry. *Ore Geology Reviews*, 145, 104909.
- Zhao, Y.M., Lin, W.W., Bi, C.S., Li, D.X. & Jiang, C.J. (1990) *Skarn deposits of China*. Beijing: Geological Publishing House, pp. 1–354.
- Zhu, Q.Q., Xie, G.Q., Mao, J.W., Hou, K.J., Sun, J.F. & Jiang, Z.S. (2017) Formation of the Jinshandian Fe skarn ore field in the Edong district, eastern China: constraints from U–Pb and ⁴⁰Ar/³⁹Ar geochronology. *Ore Geology Reviews*, 86, 1–20.

SUPPORTING INFORMATION

Additional supporting information can be found online in the Supporting Information section at the end of this article.

How to cite this article: Zhang, F., Williamson, B.J., Ullmann, C.V. & Hughes, H.S.R. (2023) Chemical changes during endoskarn and porphyry-style alteration and Cu–Fe exoskarn mineralization in the Tonglushan system, eastern China. *Resource Geology*, 73(1), e12319. Available from: <https://doi.org/10.1111/rge.12319>